

# EVOLUTION AND COLOR-DEPENDENCE OF THE GALAXY ANGULAR CORRELATION FUNCTION: 350,000 GALAXIES IN 5 SQUARE DEGREES

ALISON L. COIL<sup>1</sup>, JEFFREY A. NEWMAN<sup>2</sup>, NICK KAISER<sup>3</sup>, MARC DAVIS<sup>1</sup>, CHUNG-PEI MA<sup>1</sup>, DALE D. KOCEVSKI<sup>3</sup>, DAVID C. KOO<sup>4</sup>

*Accepted for publication by ApJ*

## ABSTRACT

When applied to deep photometric catalogs, the two-point angular correlation function,  $\omega(\theta)$ , is a sensitive probe of the evolution of galaxy clustering properties. Here we present measurements of  $\omega(\theta)$  as a function of  $I_{AB}$  magnitude and  $(R - I)$  color to a depth of  $I_{AB} = 24$  on scales  $\theta = 7'' - 3'$ , using a sample of  $\sim 350,000$  galaxies covering 5 degrees<sup>2</sup> in total over 5 separate fields. Using redshifts of 2954 galaxies in early DEEP2 Galaxy Redshift Survey data, we construct robust galaxy redshift distributions as a function of  $I_{AB}$  magnitude and  $(R - I)$  color for galaxies between  $0 < z < 2$ . We constrain models of the redshift evolution of galaxy clustering and find that significant growth of clustering has occurred from  $z \geq 1$  to  $z = 0$ . A model in which the comoving scale-length,  $x_0$ , evolves linearly with redshift,  $x_0(z) = x_0(0)(1 - Bz)$ , fits the data better than the  $\epsilon$  model proposed by Groth & Peebles (1977). The clustering properties depend strongly on observed  $(R - I)$  color, with both the reddest and bluest galaxies exhibiting large clustering amplitudes and steeper slopes. Different observed  $(R - I)$  color ranges are sensitive to very disparate redshift regimes. Red galaxies with  $(R - I) \sim 1.5$  lie in a narrow redshift range centered at  $z \sim 0.85$  and have a comoving scale length of clustering at  $z = 0.85$  of  $x_0 = 5.0 \pm 0.3 h^{-1}$  Mpc. These galaxies have early-type spectra and are likely progenitors of massive local ellipticals. The bluest galaxies with  $(R - I) \sim 0$  appear to be a mix of star-forming galaxies, both relatively local ( $z \sim 0.3 - 0.6$ ) dwarfs and bright  $z > 1.4$  galaxies, and broad-line AGN. We find that local blue dwarfs are relatively unclustered, with  $x_0 = 1.6 \pm 0.2 h^{-1}$  Mpc. The  $z > 1.4$  blue galaxies have a larger clustering scale-length,  $x_0 \gtrsim 5 h^{-1}$  Mpc.

*Subject headings:* galaxies: statistics — galaxies: evolution — cosmology: large-scale structure of universe

## 1. INTRODUCTION

Studies of galaxy clustering can constrain cosmological parameters as well as galaxy formation models, since the observed galaxy clustering strength depends on both the underlying dark matter distribution and the efficiency of galaxy formation inside dark matter halos. While theory and simulations both provide detailed predictions for the dark matter distribution in various cosmological models, the processes of galaxy formation and evolution are less well-understood. The redshift dependence of the galaxy clustering strength, in particular, can be used to constrain galaxy evolution theories if the cosmology is known.

Galaxy clustering is ideally studied in three dimensions, where the redshift of each galaxy is known. However, cosmic variance dictates the need for very large data samples, probing a large volume of space and sampling multiple independent fields, in order to obtain statistically robust results. As photometric data exist over larger areas and to fainter magnitude limits than are currently available for spectroscopic samples, galaxy clustering has long been measured from two-dimensional pho-

tometry alone.

The angular two-point correlation function,  $\omega(\theta)$ , measures the excess probability above random of finding a galaxy at a specific angle  $\theta$  from another galaxy. This quantity is derived from counts of galaxy pairs as a function of their separation, and while relatively straightforward to measure, its interpretation is not trivial. From the projected angular two-point correlation function,  $\omega(\theta)$ , one can infer the three-dimensional spatial two-point correlation function,  $\xi(r)$ , if the redshift distribution of the sources in each sample is well-known and the redshift dependence of the clustering strength is known or assumed. The two-point correlation function,  $\xi(r)$ , is usually fit as a power law,  $\xi(r) = (r/r_0)^{-\gamma}$ , where  $r_0$  is the scale-length of the galaxy clustering. However, the assumed galaxy redshift distribution ( $dN/dz$ ) has varied widely in different studies, such that similar observed angular clustering results have led to widely different conclusions. A further complication is that each sample usually spans a large range of redshifts and is magnitude-limited, such that the mean intrinsic luminosity of the galaxies is changing with redshift within a sample. As the clustering properties of galaxies are expected to depend on luminosity and have been shown to do so locally (Norberg et al. 2001), this can hinder interpretation of the evolution of clustering measured in  $\omega(\theta)$  studies.

Many of the first useful measurements of large-scale structure were studies of angular clustering. One of the earliest measurements of the  $\omega(\theta)$  statistic was the pioneering work of Peebles (1975) using photographic plates from the Lick survey. They found  $\omega(\theta)$  to be well fit by a

<sup>1</sup> Department of Astronomy, University of California, Berkeley, CA 94720 – 3411

<sup>2</sup> Hubble Fellow; Institute for Nuclear and Particle Astrophysics, Lawrence Berkeley National Laboratory, Berkeley, CA 94720

<sup>3</sup> Institute for Astronomy, University of Hawaii, 2680 Woodlawn Drive, Honolulu, HI 96822

<sup>4</sup> University of California Observatories/Lick Observatory, Department of Astronomy and Astrophysics, University of California, Santa Cruz, CA 95064

power law,  $\omega(\theta) = A_\omega \theta^\delta$ , with a slope of  $\delta = -0.77 \pm 0.06$ . Later studies using CCDs were able to reach deeper magnitude limits and found that fainter galaxies had a lower clustering amplitude. However, most of these surveys covered only one or two fields, typically with a field of view of  $\sim 50$  arcmin<sup>2</sup> due to the small sizes of CCDs, and were strongly affected by cosmic variance (e.g., Efsthathiou et al. 1991; Roche et al. 1993; Brainerd, Smail, & Mould 1995; Hudon & Lilly 1996; Woods & Fahlman 1997; McCracken et al. 2000).

More recently, wide-field cameras on intermediate-class telescopes have led to deep wide-field photometric surveys (e.g., Neuschaefer & Windhorst 1995; Roche & Eales 1999; Cabanac, de Lapparent, & Hickson 2000; McCracken et al. 2001; Wilson 2003). A ground-breaking study was conducted by Postman et al. (1998), who used a 4-m telescope with a 16 arcmin field of view to cover a much wider area by tiling together several pointings, surveying a contiguous  $4 \times 4$  degree<sup>2</sup> field to a depth of  $I_{AB} = 24$ , reaching to  $z \sim 1$ . McCracken et al. (2001) present a survey of 1 degree<sup>2</sup> to a depth of  $I_{AB} = 25.5$  over four independent fields using the UH8K camera on CFHT, and Wilson (2003) use the same camera to image 1.5 degrees<sup>2</sup> over 3 separate fields to a depth of  $I = 24.0$ .

Other recent studies employ accurate photometric redshifts to measure  $\omega(\theta)$  for galaxy samples of a specific type over well-defined redshift ranges. Brown et al. (2003) investigate the clustering of red galaxies in three redshift bins between  $0.3 < z < 0.9$  in a 1.2 degree<sup>2</sup> field from the NOAO Deep Wide-Field Survey (Jannuzi & Dey 1999), while Budavari et al. (2003) use data from the Sloan Digital Sky Survey (SDSS, York et al. (2000)) to construct a volume-limited sample with more than 2 million galaxies between  $0.1 < z < 0.3$  with which to study galaxy clustering as a function of color and spectral type.

In this paper we present a survey undertaken with the CFH12K camera covering a total of 5 degrees<sup>2</sup> over 5 separate fields to a depth of  $I_{AB} = 24.0$ . There is a wide diversity of adopted redshift distributions for magnitude-limited samples in the literature, which can lead to different interpretations of similar results. Here we use much improved  $dN/dz$  distributions, relying on recent data from the DEEP2 Galaxy Redshift Survey. Unlike previous studies, we require no spectral modelling in fitting for these  $dN/dz$  distributions and no assumptions are made about the evolution of the galaxy population.

An outline of the paper is as follows. In Sections 2 and 3 we describe the observations and data reduction process. As a large subset of this data was used for the DEEP2 Galaxy Redshift Survey photometry, we provide a detailed account of the data reduction pipeline. In section 4 we present galaxy counts in three photometric bands, while in Section 5 we measure  $\omega(\theta)$  as a function of  $I_{AB}$  magnitude, describe the  $dN/dz$  distributions we use and discuss constraints on the evolution of galaxy clustering. Section 6 parallels Section 5 but focuses on clustering as a function of  $(R - I)$  color. In this section we discuss in particular the strong clustering seen for the reddest and bluest galaxies and discuss the most likely interpretations of this effect. We conclude in Section 7.

## 2. OBSERVATIONS

Our data were taken using the CFH12K camera on the 3.6-m Canada-France-Hawaii telescope. The CFH12K camera has a  $12,288 \times 8,192$  pixel CCD mosaic array and a plate-scale of  $0.207''$  per pixel, providing a field of view of  $0.70 \times 0.47$  degrees. We observed five separate fields on the sky, with one to five distinct CFH12K pointings per field, where the area in one pointing equals the field of view of the camera. Our data were taken during several observing runs from September 1999 to October 2000 and with queue-scheduled observing from April to July 2001; observing details are given in Table 1.

We integrated on each pointing for  $\sim 1$  hour in  $B$  and  $R$  and  $\sim 2$  hours in  $I$ , broken down to individual exposures of 600 seconds. We dithered the telescope slightly between exposures to fill in gaps between the CCDs and to cover areas with low charge transfer to yield well-sampled combined images. We also took four additional 120-second  $I$ -band astrometry images in each pointing, with offsets of  $3.5'$  in RA and  $7'$  in Dec. between images. The seeing varied from  $0.69''$  to  $0.95''$ , with final seeing estimates for each pointing listed in Table 1.

## 3. DATA REDUCTION

### 3.1. Initial Processing

The data were reduced using the C-based IMCAT software package developed by Nick Kaiser<sup>5</sup>. After bias-subtracting each exposure, we constructed a super-flat for each passband from the median of the science images, which were individually normalized by the mode. The super-flats were adjusted by applying a multiplicative correction to each chip (aside from one chip arbitrarily chosen as a reference) such that when divided into the science data frames they resulted in a near constant sky level across the entire focal plane. We then created mask images which masked out saturated stars, regions with bad charge transfer and other CCD defects. After dividing each exposure by the appropriate super-flat we applied the mask images. A model for the sky level in each exposure was then obtained by estimating the local mode using a set of  $8 \times 16$  sub-images of size  $256 \times 256$  pixels and smoothly interpolating between these points using triangular tessellation (very discrepant values, e.g. around bright stars, were rejected). We then created initial catalogs of objects from each of the sky-subtracted images, computing magnitudes using a 20-pixel radius aperture, which is large enough to be unaffected by variations in the seeing, but not so large that systematic errors in flux from uncertainty in the background sky level dominate. From these catalogs we selected stars in each exposure, for both the astrometric and science images, selecting compact, bright objects. The star catalogs from the astrometry images were then used to determine astrometric solutions for our dataset.

### 3.2. Astrometry

We used the US Naval Observatory catalog (USNOA 2.0) as an absolute astrometric reference system. In each pointing, we used stars which were detected in both the USNOA catalog and in at least one of our four astrometry images to determine a set of true star positions from which we fit (rejecting outliers) cubic polynomial distortion parameters for each of the 4 exposures  $\times$  12 chips.

<sup>5</sup> <http://www.ifa.hawaii.edu/~kaiser/imcat/>

The resulting rms errors are approximately  $0''.006$ , as shown in Figure 1, where we plot the residuals in pixel coordinates of the stellar positions from the best-fit solutions. These are our relative astrometric errors; our absolute errors are defined by the accuracy of the USNOA catalog, which is roughly  $0.5''$ .

We then used these field distortion models to compute the amplification associated with the distortion as a function of position on the focal plane. This can in turn be used as a check of our astrometry solutions; we expect the amplification to be a simple quadratic function of radius, such that gross deviations from this form would most likely indicate systematic errors (feeding in from the large-scale systematic errors in the USNOA catalog). The field distortion amplifications were also needed to correct the stellar magnitudes. We found that the field distortion conformed well to the expected circularly symmetric quadratic behavior, and we conclude that systematic errors in our astrometry are very small. After solving for the astrometric solution between the astrometry images and the USNOA catalog, we fit for astrometric solutions between the science exposures for each pointing and the astrometric exposures, again using catalogs of stars selected by size and magnitude.

### 3.3. Initial Photometry

Each science exposure yielded a catalog of  $\sim 800 - 1000$  stars. The stellar magnitudes were corrected for field-distortion amplification, and the catalogs of each pair of exposures were merged using the sky coordinates provided by the astrometric solution. This provided a very large set of pairs of measured stellar magnitudes, along with the chip numbers, detector coordinates and exposure numbers. We then fit, by least squares minimization, a model in which the magnitude of an object measured on chip  $c$  in exposure  $e$  is  $m_{ce} = m + dm_c + dm_e$ . This method simultaneously measures corrections for extinction terms in individual exposures ( $dm_e$ ) as well as chip-to-chip zeropoint offsets ( $dm_c$ ). The extinction values fit were generally very small, typically  $\sim 0.005$  magnitudes, indicating that conditions were accurately photometric, but much larger values were found for the chip correction factors  $dm_c$ , ranging up to  $\sim 0.05$  mag. This is not surprising, as the CCDs in the CFHT12K are an inhomogeneous collection, with substantial variations in the quantum efficiency. The resulting error at bright magnitudes ( $16.5 < m < 18.0$ ) is  $\langle (m_1 - m_2)^2 \rangle^{1/2} \approx 0.02$  mag, as shown in Figure 2. At fainter magnitudes, the scatter is larger due to measurement error. These results show that with this simple correction the magnitudes for stars are highly reproducible exposure-to-exposure with an error  $\sim 0.02/\sqrt{2}$ .

Finally, we combined the individual science exposures for a single pointing, deleting cosmic rays, correcting for the field distortion, and creating a set of  $9 \times 13$  sub-images of size  $1024 \times 1024$  pixels ('quilts'). For each quilt, we first determined which input images contributed; then the appropriate sub-images were generated and combined into a set of image planes. These were median-combined, with rejection of discrepant pixels.

### 3.4. Catalog Construction

Object catalogs were constructed for each quilt image using the faint object detection algorithm described in

Kaiser, Squires, & Broadhurst (1995). We smoothed the  $R$ -band images (the deepest obtained) with a sequence of 'Mexican hat' filters of progressively larger size, tracked the peak trajectories through the three-dimensional space of  $x$ ,  $y$ , and Gaussian radius, and then defined an object to be the peak of the significance (the height of the peak divided by the rms fluctuation for that smoothing scale) along the trajectory. We used a filter which is a normalized Gaussian of scale  $r_g$  minus a normalized concentric Gaussian of scale  $2r_g$ . The filter scale was varied from 0.5 to 20.0 pixels with equally spaced logarithmic intervals  $\Delta r_g = 0.2r_g$ ; the best-fit value of  $r_g$  provides an excellent estimate of the Gaussian radius of an object on the sky, with smaller fractional scatter (for stars) than either the half-light or Petrosian radii measured by IMCAT. We therefore use  $r_g$  as our measure of object size throughout the remainder of this paper. Note that because of the limits of the grid, objects with  $r_g > 20$  pixels will be poorly measured; however, this is of little consequence in the magnitude ranges considered here. All objects with significance  $\nu > 4$  were output to an initial object catalog; we then perform photometry for each object in four different circular apertures (of radius  $3r_g$ ,  $6r_g$ ,  $1''$ , and  $2''$ ) in each band.

Unfortunately, the algorithm used to find objects can produce false detections due to instrumental features such as diffraction spikes, bleed trails, regions of scattered light, etc. To remedy this, we developed separate IDL software to identify the problematic pixels on the projected, combined CFHT12k images; this is done separately in  $B$ ,  $R$ , and  $I$ . Our algorithm begins by flagging all saturated pixels, along with the central pixels of all partially-saturated sources identifiable in the initial object catalog; this limit is found empirically in each pointing as the magnitude where the measured sizes of stars are no longer independent of their flux. Then, all pixels less than 3 pixels from a flagged point in both  $X$  and  $Y$  for which the flux (after smoothing with a 3-pixel boxcar) is more than 3.25 times higher than the sky noise (also after smoothing, from the IMCAT sky inverse variance map) are themselves flagged as bad. This procedure is iterated until there are no pixels with significant flux within 3 pixels of a flagged pixel. In what follows, all objects whose centers are within 10 pixels of any flagged pixel (or pixel with no data, e.g. due to edges or bad pixels in the detector) in any band are rejected from analysis; this radius corresponds to  $\sim 4r_g$  for a typical object, and thus is larger than the final apertures used. The bad pixel masks produced by this procedure are also employed in masking the random catalogs used for correlation analyses (see Section 5.1).

We found by visual inspection of the resulting masked catalog that occasionally there were spurious or incorrect entries, either due to overlapping objects, where substructure within a large, extended object is detected as a small separate object within its bounds, or "overmerged" pairs or triplets of galaxies which were identified incorrectly as one extended object. To rectify these situations, we applied two algorithms, one to delete overlapping objects and one to split merged objects. For the overlapping objects, we first define a 'small' radius,  $r_s = 0.85r_{seeing}$ , and then flag as spurious any objects with  $r_g < r_s$  and which are inside  $3r_g$  of a bright, extended object or that have  $r_g < 1.5 * r_s$  and are within

$3r_g$  of a bright, extended source and have peak counts more than 2 sky sigma below the peak of the nearby background (i.e. lie on a very strong gradient background). For all tests of object overlap, we use ellipsoids with  $r_g/3r_g$  as the semimajor axis, which matched visual morphologies well. As a part of this routine, we also eliminate from the catalog identical overlapping objects identified on multiple quilts.

For the over-merged objects, we first flag all low surface-brightness (LSB), elongated objects, with  $b/a \lesssim 0.5$ , as many of these are multiples which have been incorrectly designated as a single object. Around each flagged object we smooth the image quilts with a Gaussian kernel of  $\sigma = 0.67\sigma_{seeing}$  and find all peaks within a 2-pixel radius circle which are greater than five times the sigma of the smoothed sky (i.e., the highest surface brightness regions present). We then centroid on these and measure their FWHM on the image quilt. We evaluate the significance of the original object by determining whether, after masking the candidate sub-objects, a fit to an elliptical-Gaussian model has an amplitude greater than  $5\sigma$  above 0 (where here  $\sigma$  is the uncertainty in this Gaussian-weighted amplitude). If not, we give the original object a quality flag such that it will be rejected from further use. If the significance of detection for the original object is  $> 30$ , then we consider all the high surface brightness (HSB) regions to be merely bright sub-regions of an original object, and reject them. Otherwise, for all the HSB regions, we evaluate: 1) whether they are resolvable from other HSB regions identified in this process – in case of such conflicts, we keep only the brightest peak; 2) if the HSB object is indistinguishable from a known object in the catalog – i.e. we require its distance from each known catalog object be: a)  $> 1.25\sigma_{seeing}$  from the catalog object, such that separation of the peak is resolved, or b) 0.67 times the catalog object profile  $\sigma$  from central object, so that we are not likely to be seeing substructure in the peak; and 3) whether the identified object in fact appears diffuse – i.e., has  $FWHM > 2.5$  times the seeing FWHM, and not identified with a catalog object. This throws out false diffuse detections due to low-level flat-field or sky-subtraction issues that are not the over-merged objects that we are trying to eliminate. All of the criteria and limits used were tuned empirically based on the actual over-merging of objects seen. We found that  $\sim 3\%$  of the objects were “over-merged” and were thus split into separate objects, on which we performed photometry in all three bands. As colors are computed in  $1''$  apertures, biases in the colors due to blending of sources are minimized.

### 3.5. Star-Galaxy Separation

The magnitude range of our data spans a regime where stars are a non-negligible contaminant for a galaxy catalog. Unfortunately, size and magnitude alone are not always sufficient to distinguish stars from galaxies, especially at fainter magnitudes where small intrinsic sizes and uncertainties in size measurements cause some galaxies to have measured sizes comparable to those of stars. We have therefore developed a set of algorithms which distinguish stars from galaxies in a probabilistic fashion, using their sizes, magnitudes, and  $(B - R)$ ,  $(R - I)$  colors. We exploit the fact that stars and compact galaxies have very different magnitude distributions, with stars

dominating at bright magnitudes and galaxies at faint magnitudes, and that stars fall within a tight locus in color-color space. Objects which are clearly extended, with  $r_g > 0.05$  above the upper limit of the locus of stars in the size-magnitude plane, are deemed galaxies, while compact objects are given a probability, in a Bayesian sense, of being a galaxy given their magnitude  $m$  and color vector  $\mathbf{c}$ :

$$p_{gal}(m, \mathbf{c}) = \frac{p(\mathbf{c}|gal)p(gal|m)}{p(\mathbf{c}|gal)p(gal|m) + p(\mathbf{c}|star)p(star|m)}. \quad (1)$$

The magnitude distribution of compact objects is essentially linear at the bright end ( $R \lesssim 21$ ) and rises exponentially at fainter magnitudes. We assume, quite reasonably, that the linear component is due exclusively to stars, while galaxies cause the exponential increase at the faint end. In each pointing, we perform a non-linear least-squares fit to the magnitude distribution function  $n(m) = a_0 e^{a_1 m} + a_2 + a_3 m$ , where  $m = m_R - 22$ . We then define the probability of a compact object being a galaxy, based on its magnitude, as  $p(gal|m) = (a_0 e^{a_1 m})/n(m)$ , with  $p(star|m) = 1 - p(gal|m)$ . In practice we limit the range for these priors, confining them to the range 5%-95%, in order to restrain the influence of any errors in our assumptions. It then remains to determine the color distributions of stars and galaxies.

It is first necessary to bring all pointings to a common color system. We do an initial, rough calibration using observed number counts; in the absence of cosmic variance, the number of galaxies within a given magnitude range should be the same in each pointing and bandpass. We can refine the zeropoints of our color system by forcing the locus of stars, chosen for their compact size and bright magnitudes, for the first iteration of this procedure, in color-color space to match amongst all pointings. This locus is well-approximated in our bands by two intersecting line segments of fixed slope; therefore, by fitting the color distribution of stars in each pointing to that functional form, via least-squares minimization, we may derive the offset in both  $(B - R)$  and  $(R - I)$  colors required to make the stellar locus match our reference pointing. We chose pointing 2 in field 2330 (see Table 1) to be our reference pointing, for reasons described below. This procedure indicates that the color zeropoints derived from number counts are consistent from pointing to pointing to within 0.03 mag rms in  $(R - I)$  and 0.05 mag rms in  $(B - R)$ . By using the stellar locus, although we do not necessarily know the correct absolute zeropoint in any pointing in any band, we can bring all pointings to a common color system in a robust way. We iteratively repeat this stellar locus calibration as the color distributions of stars and galaxies are refined, using the probabilistic star-galaxy separation defined above after the first color distributions are constructed; excellent convergence occurs within two iterations. In addition, we use the variations in the stellar locus within subregions of each individual pointing to derive a smooth correction for residual scattered light and/or flat field errors, applied using a minimum-curvature surface interpolation.

After bringing all pointings to a common color system, we select objects within a pointing which are: 1) almost certainly stars (i.e., that have  $r_g$  within the stellar range, and either  $19 < m_R < 21.25$ , or  $m_R < 24$ ,

( $R - I$ )  $> 1.45$ , and color within  $\pm 0.2$  mag of the expected stellar locus – this latter requirement is necessary to include M stars), 2) bright compact galaxies ( $20.5 < m_R < 23.5$ ,  $r_g$  larger than the stellar range but less than  $\sqrt{(1.5pix)^2 + r_{seeing}^2}$ ), or 3) faint compact galaxies ( $m_R > 23.5$  and  $r_g$  as above). Plots of the positions for compact galaxies and stars in ( $B - R$ ) and ( $R - I$ ) space for data in one pointing are shown in Figure 3.

We then create a two-dimensional color-color histogram for each of these samples, which we smooth by a two-dimensional Gaussian kernel with a  $\sigma = 0.05$  mag to take into account the effects of magnitude errors in applying these distributions to catalog objects. We delete outliers, redo the smoothing, and normalize the distributions to have a maximum probability of one. This results in a probability distribution for the color of stars directly, though for galaxies we have to take into account the magnitude-dependence of their distribution in color-color space, so as not to be dominated by the more numerous, faint objects. We therefore define  $p(\mathbf{c}|gal) = w(m_R)p(\mathbf{c}|bright) + (1 - w(m_R))p(\mathbf{c}|faint)$ , where *bright* and *faint* denote the two galaxy samples we defined above and  $w = 1$  for  $m_R < 23$ ,  $w = m_R - 23$  for  $23 < m_R < 24$  and  $w = 0$  for  $m_R > 24$ . We then use equation 4 to determine the probability for each compact object that it is a galaxy.

We emphasize that we have computed color-color distributions for the bright and faint compact objects separately; we are not assuming that galaxy colors and magnitudes are completely independent. It is primarily important in our Bayesian method that the color distribution of galaxies – our prior – fills a different space than the stellar color distribution. And as galaxies of a given redshift and restframe color have substantial breadth to their luminosity function, the covariance between color and magnitude is dilute. A full treatment of the three-dimensional distribution of magnitude and color would greatly complicate implementation and would yield noisy results at bright magnitudes where we have fewer galaxies to build a distribution from, but also where star-galaxy separation is most important. The resulting strong separation between stars and galaxies that we find using our probabilistic method shows that we are not sensitive to such details.

We find that 68% of the objects are extended, while 2% do not have sufficient information to determine  $p_{gal}$ , either because they lack data in one or more passbands or are brighter than the saturation limit. Figure 1 shows the  $p_{gal}$  distribution for the *compact* objects, which is extremely bi-modal, with 25% of the objects having 0% probability of being a galaxy and 38% having 100% probability of being a galaxy. The few objects with intermediate values of  $p_{gal}$  tend to lie near these extremes, and so in the analyses of angular correlations that follow we include only those objects with a  $> 20\%$  probability of being a galaxy, though it makes very little difference what exact cutoff is used. Effects on the angular clustering measurements due to stellar contamination are discussed in section 5.2.

### 3.6. Final Photometry

A large portion of the photometry presented here is used by the DEEP2 Galaxy Redshift Survey Davis et al. (2002), and as a courtesy we define the photometric calibrations such that they are optimal for that survey. We therefore define a set of magnitudes in the AB system, with a total,  $R_{AB}$ -band magnitude and ( $B - R$ ), ( $R - I$ ) colors for each object. We adopt as our measure of total magnitude the  $R$  magnitude measured in a circular aperture of radius  $3r_g$ , unless  $3r_g$  is less than  $1''$  (due to noise in its measurement), in which case we use the magnitude within a  $1''$  radius. We found that the magnitude within  $6r_g$  as measured by IMCAT is often contaminated by nearby objects included within the aperture or problematic as the aperture goes beyond the buffer region of each quilt for objects near their edges, while the  $3r_g$  magnitude proved more robust.

Conventionally, we would then use the  $B$  and  $I$  magnitudes measured within this same aperture to define our system; however, due to differences in seeing/aperture corrections between bands and amongst the CFHT12k pointings, it would then be impossible to make the colors of extended objects (i.e. galaxies) agree pointing-to-pointing even if the colors of the stellar locus match; this effect can reach  $\sim 0.05$  mag in each band. This effect is much smaller for colors derived from the IMCAT  $1''$  aperture magnitudes,  $\lesssim 0.02 - 0.03$  mag in both ( $B - R$ ) and ( $R - I$ ), based on cross-correlating the color locus of extended objects from pointing to pointing. Therefore, we adopt as the basis of our magnitude system the quantities we can measure and calibrate most robustly: the “total”  $R_{AB}$  magnitude, measured in the  $3r_g$  aperture, and the two colors ( $B - R$ ) and ( $R - I$ ), each measured within  $1''$  apertures. In the remainder of this paper,  $B$  will be used to represent  $R_{total} + (B - R)_{1''}$ , and  $I$  will represent  $R_{total} - (R - I)_{1''}$ . Note that these should be distinct from conventional magnitudes only in the case of resolved color gradients within the observed galaxies.

We calibrate our  $R_{AB}$ -band magnitude and ( $B - R$ ), ( $R - I$ ) colors through two separate processes. First, we calibrate  $B$ ,  $R$ , and  $I$  to an AB magnitude system in the native CFHT12k passbands using SDSS photometry for stars in our reference pointing (pointing 2 in field 2330 [see Table 1]). This pointing was chosen to define our color system as it yielded the cleanest comparison to SDSS, due to the quality both of the CFHT12k observing conditions and the SDSS photometry (it lies on the celestial equator and has been observed by SDSS repeatedly). The accuracy of this calibration is  $\sim 0.02 - 0.03$  mag (worst in  $B$ ), dominated by errors in the SDSS calibration. Through iteratively fitting the stellar locus, bringing all pointings to a common color system, determining the overall color distributions of stars and galaxies, and reapplying our star-galaxy separation algorithm, we not only produce a stable star-galaxy separation but also bring all pointings to the same ( $B - R$ )<sub>1s</sub>, ( $R - I$ )<sub>1s</sub> color system to within  $\sim 0.01$  mag in each color; the zeropoints of that color system are then set by the SDSS calibration of our reference pointing. After our correction for spatial variations in the color system using variations in the stellar locus, residual variations in the ( $B - R$ ) and ( $R - I$ ) zeropoints within each pointing are estimated to be 0.04 and 0.03 mag, respectively; these variations should primarily be relevant on scales of  $\sim 4' - 8'$ .

Second, after this calibration of the color system has been performed, we calibrate the  $R$ -band zeropoint in each pointing. In the four pointings for which no information from SDSS is available (and which are not used in the DEEP2 Galaxy Redshift Survey), we determine zeropoints by forcing the number counts to match those from our other fields; based on pointings with SDSS calibration, we find that this yields a zeropoint with errors of 0.10 mag, due to cosmic variance (errors from this technique in  $(B - R)$  or  $(R - I)$  are smaller as the cosmic variance is strongly covariant between bands). We have tested several of the below analyses with and without the inclusion of these less-calibrated pointings, and all differences were well within the quoted errors. In the fields with SDSS calibration, however, by comparing  $B$ ,  $R$ , and  $I$  to the SDSS magnitudes for stars, we get three *independent* estimates of the  $R$  zeropoint (as we have tied the three magnitudes together in our photometry by making the stellar loci match). In general, the zeropoints estimated from  $R$  and  $I$  agree to within 0.02 mag rms, while these agreed with the zeropoint from  $B$  to  $\sim 0.04$ ; this matches well the expected variation in SDSS photometric zeropoints. We use the average of the zeropoint offsets from  $R$  and  $I$  to correct our photometry wherever SDSS photometry is available. Based on comparisons to SDSS, residual variations of the  $R$  zeropoint within each pointing, which we cannot correct for with either the stellar locus or number counts, appear to be  $\lesssim 0.02$  mag rms. The final uncertainty in the absolute calibration includes both a random error due to the finite number of stars with well-measured magnitudes in both datasets and a systematic error due to uncertainties in the AB magnitude calibration of the SDSS photometry.

#### 4. GALAXY COUNTS

We first present galaxy number counts for our data in order to test the uniformity and depth of the sample. Figure 5 shows histograms of  $B_{AB}$ ,  $R_{AB}$  and  $I_{AB}$  galaxy counts for all 15 pointings, in units of log number of counts per degree<sup>2</sup> per 0.5 magnitude. At the bright end we see variations in the counts due to cosmic variance, while at the faint end the varying depth of the data in each pointing leads to differences in the counts past our completeness limit. Our data is complete to  $\sim 24.5$  in  $B_{AB}$ ,  $\sim 24.0$  in  $R_{AB}$ , and  $\sim 23.5$  in  $I_{AB}$  in all pointings except field 1416, pointing 2, which is our shallowest pointing and the low data point at each of the completeness limits in Figure 5. We fit for the slope in the galaxy counts,  $\delta \equiv d \log N / dm$ , in each band over the magnitude range in which the data is consistent from pointing to pointing. The  $B$ -band galaxy counts have a slope of  $\delta = 0.49 \pm 0.02$  in the magnitude range  $B_{AB} = 21 - 24$  mag. This fit is shown in the bottom of Figure 5 as the dotted line and agrees well with Brunner, Connolly, & Szalay (1999) ( $\delta = 0.51$ ,  $B_{AB} \sim 20 - 24$ ), McCracken et al. (2001) ( $\delta = 0.47 \pm 0.02$ ,  $B_{AB} = 20 - 24$ ) and McCracken et al. (2003) ( $\delta = 0.45 \pm 0.01$ ,  $B_{AB} = 20 - 24$ ). Our  $R_{AB}$  galaxy counts have a slope of  $\delta = 0.36 \pm 0.01$  in the magnitude range  $R_{AB} = 20 - 24$  mag, in agreement with Hogg et al. (1997), Brunner, Connolly, & Szalay (1999), Metcalfe et al. (2001) and McCracken et al. (2003) who find slopes of  $\delta = 0.33, 0.34, 0.37$ , and  $0.37 \pm 0.03$ , respectively. Our  $I_{AB}$  counts have a slope of  $\delta = 0.32 \pm 0.01$  in the magnitude range  $I_{AB} = 21 - 24$

mag, which also agrees well with other published results in similar magnitude ranges, all of which report a slope between 0.31–0.35 (Brunner, Connolly, & Szalay (1999), Arnouts et al. (1999), Metcalfe et al. (2001), McCracken et al. (2001), Wilson (2003), McCracken et al. (2003)).

#### 5. GALAXY CLUSTERING AS A FUNCTION OF MAGNITUDE

In this section we present measurements of  $\omega(\theta)$  as a function of  $I_{AB}$  magnitude and use redshift distributions of galaxies from the early DEEP2 Galaxy Redshift Survey data to constrain models of clustering evolution. Section 6 presents a parallel study of galaxy clustering as a function of  $(R - I)$  color.

##### 5.1. The Angular Two-point Correlation Function

The projected angular two-point correlation function  $\omega(\theta)$  is a measure of the probability above Poisson of finding two galaxies with a separation  $\theta$ , defined as

$$dP = N[1 + \omega(\theta)]d\Omega \quad (2)$$

where  $N$  is the mean number of galaxies per steradian and  $d\Omega$  is the solid angle of a second galaxy at a separation  $\theta$  from a randomly chosen galaxy. To measure  $\omega(\theta)$  one must first construct a catalog with a random spatial distribution and uniform density of points with the same selection criteria as the data, to serve as an unclustered distribution with which to compare the data. For each of our 15 pointings we created a random catalog with 200,000 points (17 times larger than the largest data sample we use here) with the same sky coverage as our data, for which we then applied the same masking that was used to mask bad regions of the data due to saturated stars and CCD defects.

We measure  $\omega(\theta)$  using the Landy & Szalay (1993) estimator,

$$\omega(\theta) = \frac{1}{RR} \left[ DD \left( \frac{n_R}{n_D} \right)^2 - 2DR \left( \frac{n_R}{n_D} \right) + RR \right], \quad (3)$$

where  $DD$ ,  $DR$ , and  $RR$  are pair counts of galaxies in the data-data, data-random, and random-random catalogs with separation  $\theta + \delta\theta$ , and  $n_D$  and  $n_R$  are the mean number densities of galaxies in the data and random catalogs. This estimator has shown to be relatively insensitive to the size of the random catalog and handles edge corrections well (Kerscher, Szapudi, & Szalay 2000). We measure  $\omega(\theta)$  in logarithmic bins of 0.2 in  $\log(\theta)$  with  $\theta$  measured in degrees.

Measurements of  $\omega(\theta)$  are known to be low by an additive factor known as the “integral constraint” (IC, see e.g. Peebles 1980) which results from using the data sample itself to estimate the mean galaxy density. This correction becomes important on scales comparable to the survey size, here equal to 0.5 degrees, the short axis of a single CFHT12k pointing. We therefore constrain our fits to a maximum  $\theta$  of 0.05 degrees, where the IC is negligible.

##### 5.2. Galaxy Clustering as a Function of $I_{AB}$ Magnitude

Figures 6 and 7 present  $\omega(\theta)$  measured for independent magnitude bins in the range  $I_{AB} = 18 - 24$  on scales of  $\sim 7'' - 6'$ . The amplitude of the clustering is seen to

smoothly decrease with magnitude, with fainter magnitude bins showing less projected clustering. In Figure 6 one can see that  $\omega(\theta)$  approaches zero on large scales, while Figure 7 shows clearly the effects of the IC; on scales larger than  $\sim 3'$  the amplitude of  $\omega(\theta)$  begins to fall below the power-law form seen on smaller scales. In each of these plots we have measured the mean value of  $\omega(\theta)$  in each  $\theta$  bin. The error bars on  $\omega(\theta)$  are calculated from the standard error across our 15 independent pointings and should be a robust estimate of the error due to cosmic variance. We find that  $\omega(\theta)$  measured by first summing the DD, DR, and RR counts over all the pointings, and then using Equation (3) to estimate the clustering amplitude, is consistent with the mean values shown here.

For each magnitude range we fit a power-law form,  $\omega(\theta) = A_\omega \theta^\delta$ , on scales  $\sim 7'' - 3'$  and solve for the slope and amplitude using a least-squares fitting algorithm where we minimize  $\chi$ -squared, taking into account the covariance between bins as determined from bootstrap resampling. We first assume a slope of  $\delta = -0.8$  to compare with other published results. Table 2 lists the amplitude of  $\omega(\theta)$  measured at  $1'$ ,  $A_\omega(1')$ , in each magnitude bin for a slope of  $\delta = -0.8$ , along with an error from the least-squares fitting and the median number of galaxies within a single pointing in that magnitude range, equal to the median sample size. We find that the errors estimated from bootstrap resampling are nearly identical to those calculated above. In Figure 7 these fixed-slope fits are plotted as dashed lines. As can be seen in this figure, a slope of  $\delta = -0.8$  is generally consistent with the data for the magnitude ranges and scales we study here.

In Figure 8 we plot the amplitude of  $\omega(\theta)$  at  $1'$ ,  $A_\omega(1')$ , as a function of median  $I_{AB}$  magnitude for an assumed slope of  $\delta = -0.8$ . Our values agree well with the recent results of McCracken et al. (2001) (who do not use independent magnitude bins, but always keep a bright limit of  $I_{AB} = 18.5$  and vary the faint limit of their magnitude range) and with Wilson (2003), though our data points are slightly lower (see Wilson (2003) for a figure comparing their data with other results in the literature). However, our results do not agree well with Brainerd, Smail, & Mould (1995), Woods & Fahlman (1997), or Postman et al. (1998), who all find significantly higher amplitudes at faint magnitudes,  $I_{AB} > 22$ . The surveys of both Brainerd, Smail, & Mould (1995) and Woods & Fahlman (1997) are quite small, covering less than 150 arcmin<sup>2</sup> each, and are therefore subject to significant cosmic variance. Postman et al. (1998) cover a very wide area (16 degrees<sup>2</sup>) separated over 256 contiguous individual pointings. We find that their values of  $\omega(\theta)$  are a factor of two higher than our measurements at  $I_{AB} \sim 22$ . It is unlikely that this large of a discrepancy could be caused primarily by errors on their estimates of the IC, which would only affect larger scales than we are considering here, or by errors in stellar contamination estimates, which would have to be unreasonably large at these magnitudes. A much more likely explanation is that these differences may be the result of calibration errors in their photometry, as any zero-point differences across their pointings would lead to a systematic increase in the measured clustering on all scales, as pairs across pointings are used on even the smallest scales. This would also have a greater effect at fainter magnitudes, where the relative photometric er-

ror is larger. Here we measure  $\omega(\theta)$  only within individual pointings and do not attempt to compute  $\omega(\theta)$  across pointings. The continued decrease in clustering which we find for fainter galaxies is also seen by McCracken et al. (2001) and Wilson (2003).

As can be seen in Figure 7, the canonical slope of  $\delta = -0.8$  does not fit the data exactly at all magnitudes, and so we next relax the assumption of a fixed slope and measure both the slope and amplitude of  $\omega(\theta)$  for each magnitude bin on scales of  $\sim 7'' - 3'$ . The resulting slope as a function of median  $I_{AB}$  magnitude is shown in Figure 9 and listed in Table 2, along with the amplitude,  $A_\omega(1')$ . The slope varies between  $\delta \sim -0.7 - -1.0$ , with a maximum between  $I_{AB} \sim 19 - 21$  and shallower values at fainter magnitudes. As shown in Figure 9, our values are consistent with those of McCracken et al. (2001), and the general trend we find in how the slope varies with magnitude is consistent with Postman et al. (1998), though they measure shallower slopes at all magnitudes. Wilson (2003) report that a slope of  $\delta = -0.8$  fits their data well for the magnitude range  $I_{AB} = 20 - 24$ .

A decrease in the slope of  $\omega(\theta)$  at fainter magnitudes implies evolution in the slope of  $\xi(r)$ , such that the slope is shallower at higher redshift. Semi-analytic models predict a decrease in the slope of  $\xi(r)$  from  $\sim 1.85$  at  $z \sim 0$  to  $\sim 1.6$  at  $z \sim 1$  (Kauffmann et al. 1999), and measurements of  $\xi(r)$  in early data from the DEEP2 Galaxy Redshift Survey have a slope of  $\gamma = -1.66 \pm 0.12$  (Coil et al. 2004). These results presented here are consistent with a similar decrease in the slope at  $z \sim 1$  (see Section 5.4 for a discussion of the redshift distribution as a function of magnitude).

### 5.3. Modelling $\omega(\theta)$

As the two-dimensional galaxy clustering seen in the plane of the sky is a projection of the three-dimensional clustering,  $\omega(\theta)$  is directly related to its three-dimensional analog  $\xi(r)$ . For a given  $\xi(r)$ , one can predict the amplitude and slope of  $\omega(\theta)$  using Limber's equation, effectively integrating  $\xi(r)$  along the redshift direction (e.g. Peebles 1980). If one assumes  $\xi(r)$  (and thus  $\omega(\theta)$ ) to be a power-law over the redshift range of interest, such that

$$\xi(r, z) = \left[ \frac{r_0(z)}{r} \right]^\gamma, \quad (4)$$

then

$$w(\theta) = \sqrt{\pi} \frac{\Gamma[(\gamma - 1)/2]}{\Gamma(\gamma/2)} \frac{A}{\theta^{\gamma-1}}, \quad (5)$$

where  $\Gamma$  is the usual gamma function. Here we use the convention of  $r$  being a physical length, and  $x$  being a comoving length, such that  $r = ax$ , where  $a$  is the scale factor. We therefore quote the comoving scale-length of clustering as a function of redshift as  $x_0(z)$  and the local value as  $x_0(0)$  (equal to  $r_0(0)$ ). The amplitude factor,  $A$ , is given by

$$A = \frac{\int_0^\infty x_0^2(z) g(z) \left( \frac{dN}{dz} \right)^2 dz}{\left[ \int_0^\infty \left( \frac{dN}{dz} \right) dz \right]^2} \quad (6)$$

where  $dN/dz$  is the number of galaxies per unit redshift interval and  $g(z)$  depends on  $\gamma$ , and the cosmological

model:

$$g(z) = \left(\frac{dz}{dx}\right) x^{(1-\gamma)} F(x). \quad (7)$$

Here  $x$  is the comoving distance at a redshift  $z$  and  $F(x)$  is the curvature factor in the Robertson-Walker metric,

$$ds^2 = c^2 dt^2 - a^2 [dx^2/F(x)^2 + x^2 d\theta^2 + x^2 \sin^2 \theta d\phi^2]. \quad (8)$$

If the redshift distribution of sources,  $dN/dz$ , is well-known, then the amplitude of  $\omega(\theta)$  can be predicted for a given power-law model of  $\xi(x)$ , such that measurements of  $\omega(\theta)$  can be used to place constraints on the evolution of  $\xi(x)$ .

#### 5.4. Redshift Distribution as a Function of Magnitude

In the literature there is a wide variety of adopted redshift distributions for magnitude-limited samples, which is alarming as the predicted amplitude of  $\omega(\theta)$  is quite sensitive to the assumed shape, and particularly the width, of the redshift distribution. Most authors use either galaxy evolution models or small observational samples ( $N \sim 100$ ) to construct  $dN/dz$  distributions. McCracken et al. (2001) use their own galaxy evolution models which are tested against an HDF sample of 120 galaxies and which reproduce the trend of median magnitude with  $z$  and dispersion in redshift for a given magnitude range as seen by the Canada-France Redshift Survey (CFRS). Cabanac, de Lapparent, & Hickson (2000) use the CFRS luminosity function combined with the PEGASE spectral atlas (Fioc & Rocca-Volmerange 1997) to construct models of the  $dN/dz$  distributions. As they point out, the choice of which atlas to use can affect the K-corrections by as much as 50%, so that their  $dN/dz$  distribution is quite sensitive to this choice. Roche & Eales (1999) use the Charlot, Worthey, & Bressan (1996) spectral evolution models combined with the luminosity function of the Las Campanas Redshift Survey data.

Other authors have used observed redshift distributions from relatively small, deep spectroscopic surveys. Postman et al. (1998) use the empirical function  $dN/dz \propto z^2 \exp[-(z/z_0)^2]$ , fit to the CFRS spectroscopic data. These fits are presumably based on the sample of  $\sim 600$  galaxies for which CFRS obtained secure redshifts, with the highest  $z \sim 1.3$ . They also use various evolving Schechter luminosity functions to model  $dN/dz$  and find parameters which provide good fits to their  $\omega(\theta)$  results. Wilson (2003) use the form  $dN/dz \propto z^2 \exp(-z/z_0)$ , where the mean redshift is  $3z_0$  and the median redshift is  $2.67z_0$ . They fit for  $z_0$  using the SSA22 field sample of Cowie, Songaila, & Barger (1999), which has  $\sim 200$  galaxies to  $I = 23.25$ , where corrections are made for faint galaxies without redshifts which are thought to lie between  $z = 1.5 - 2.0$ . This parameterization of  $dN/dz$  is markedly different from that of Postman et al. (1998), with more galaxies at higher redshift, and leads to very discrepant predictions of the amplitude of  $\omega(\theta)$  as a function of magnitude (at  $I_{AB} = 23$  the CFRS  $dN/dz$  model predicts a value of  $A_\omega$  which is 6% lower for  $\epsilon = 0$ , 14% lower for  $\epsilon = 1$ , and 23% lower for  $\epsilon = 2$ ; see Section 5.5 for a definition and discussion of  $\epsilon$ ).

Here we use a uniform sample of 2954 galaxies with secure redshifts in early DEEP2 Galaxy Redshift Survey (Davis et al. 2002; Coil et al. 2004; Madgwick et al. 2003) data in the Extended Groth Strip (EGS), where

redshifts are observed from  $z \simeq 0 - 1.5$ . We find that the form used by Wilson (2003),  $dN/dz \propto z^2 \exp(-z/z_0)$ , fits the DEEP2 data reasonably well. The overall normalization of  $dN/dz$  is irrelevant in estimating the amplitude of  $\omega(\theta)$ ; it is the shape, and particularly the width, of  $dN/dz$  that is important for our purposes. The  $dN/dz$  parameterization Postman et al. (1998) used for the CFRS data does not fit the DEEP2 sample; their narrower function contains too few objects at high redshifts.

To reconstruct the redshift distribution of sources in the DEEP2 data we have inversely weighted each galaxy by its probability of selection, which is a function of magnitude (Newman et al. 2004). Figure 10 shows the redshift distribution of sources in the DEEP2 data along with our best-fit  $dN/dz$  distribution for differential magnitude bins. As discussed in Coil et al. (2004), the DEEP2 Galaxy Redshift Survey does not measure redshifts for galaxies at  $z \geq 1.45$  as the  $\lambda 3727 \text{ \AA}$  [OII] doublet and Ca H+K absorption features move out of the observable spectral wavelength range. Therefore, any objects at  $z \gtrsim 1.45$  are not included in the sample used to derive  $dN/dz$ . This will affect the fainter magnitude ranges in particular, which will be missing objects at  $z \geq 1.45$ . Chuck Steidel has followed up our blue  $((B - R) \leq 0.4)$  failures using LRIS-B (private communication) and has found that of the 20 objects he has targeted, all were at  $z > 1.45$ , with a median  $z = 1.75$  and a standard deviation of  $\sigma \sim 0.30$ . This redshift distribution is very similar to that shown in Steidel et al. (2004) for the 'BM' galaxies, which lie at  $\langle z \rangle = 1.70 \pm 0.34$ , and it seems quite likely that our blue failures are in the 'BM' population. We correct our redshift distributions by assigning redshifts to the blue galaxies without measured redshifts such that they have a Gaussian distribution with a mean of  $z = 1.75$  and a standard deviation of  $\sigma = 0.30$ . Our resulting redshift distributions are shown in Figure 10. Fits for  $z_0$  for each magnitude range are shown in Table 3 with and without the correction for missed galaxies at  $z > 1.45$ , which affected only the fainter magnitude bins. Errors on  $z_0$  were calculated using bootstrap resampling of the data and may underestimate errors due to cosmic variance, as the 2954 redshifts which we use are from a single  $\sim 0.5 \times 0.3$  degree field.

After fitting our  $dN/dz$  model to the DEEP2 spectroscopic sample, we find that  $z_0$  is well-fit as a linear function of the median  $I_{AB}$  magnitude:  $z_0 = -0.84 + 0.050$  median  $I_{AB}$ , where the median redshift is  $2.67z_0$  and the mean redshift is  $3z_0$ . Figure 11 plots our data points for the median redshift as a function of median  $I_{AB}$  magnitude, with a solid line showing the linear fit. We also include recent results from Wilson (2003) and Brodwin et al. (2003). Wilson (2003) use the same functional form for  $dN/dz$  that we use here, though their fits of  $z_0$  vs magnitude do not match ours well at magnitudes fainter than  $I_{AB} \sim 22$ , where they find a higher median redshift than we do. However, their results are based on a small sample of  $\sim 200$  galaxies. Our results agree better with those of Brodwin et al. (2003), though they find systematically lower values for the median redshift as a function of magnitude and use a narrower  $dN/dz$  fitting form which has fewer galaxies at higher redshifts.

We also include in Table 4 fits for  $dN/dz$  in integral



magnitude ranges for both  $R_{AB}$  and  $I_{AB}$  bands, which are of interest for other analyses such as weak gravitational lensing studies. For the integral magnitude bins we fit for two distributions,  $dN/dz \propto z^2 \exp(-z/z_0)$  and  $dN/dz \propto z^2 \exp(-z/z_0)^{1.2}$ , and find that they both fit the data well to within the noise. For the  $z^2 \exp(-z/z_0)^{1.2}$  distribution, the mean redshift is  $2.09z_0$  and the median  $1.91z_0$ . Beyond our limiting magnitudes of  $R_{AB} = 24$  and  $I_{AB} = 23.5$ , we extrapolate to fainter magnitudes using a simple linear fit to the  $z_0$  values in the brighter bins. Note that all magnitudes are AB in the native CFHT 12k filter system.

### 5.5. Constraining Evolution of Clustering

Given the redshift distribution of sources, one can use measurements of  $\omega(\theta)$  to either determine  $\xi(x)$  at a given redshift, if the galaxies lie in a narrow redshift range, or parameterize the redshift-dependence of  $\xi(x, z)$  and solve for the local value of  $\xi(x, 0)$  and its evolution with redshift.

Groth & Peebles (1977) suggested the ‘ $\epsilon$ -model’ for the evolution of the two-point correlation function:

$$x_0(z) = x_0(0)(1+z)^{-(3+\epsilon-\gamma)/\gamma} \quad (9)$$

$$\xi(x, z) = \left[ \frac{x_0(0)}{x} \right]^\gamma (1+z)^{-(3+\epsilon-\gamma)} \quad (10)$$

where  $x$  is a comoving distance,  $x_0(0)$  is the local value of  $x_0(z)$  and  $\gamma$  is the slope of  $\xi(x)$ . In proper coordinates, the scale-length evolves as  $r_0(z) = r_0(0)(1+z)^{-(3+\epsilon)/\gamma}$  and  $\xi(r)$  evolves as  $\xi(r, z) = \xi(r, 0)(1+z)^{-(3+\epsilon)}$ . This model was motivated such that  $\epsilon = 0$  for clustering fixed in proper coordinates, where  $n\xi = \text{constant}$  and  $n$  is the mean galaxy density. Clustering which is fixed in comoving coordinates requires  $\epsilon = \gamma - 3$ , which equals  $-1.2$  for  $\gamma = 1.8$  (equivalent to  $\delta = -0.8$ ). Any value of  $\epsilon > 0$  leads to growth of clustering in proper coordinates. Linear theory predicts  $\epsilon = \gamma - 1$ , equal to  $0.8$  for  $\gamma = 1.8$ , for growth of dark matter clustering in an  $\Omega_M = 1$  cosmology. Using this  $\epsilon$  parameterization for the growth of clustering, equation 6 becomes

$$A = \frac{\int_0^\infty x_0^\gamma(0)(1+z)^{-(3+\epsilon-\gamma)} g(z) \left( \frac{dN}{dz} \right)^2 dz}{\left[ \int_0^\infty \left( \frac{dN}{dz} \right) dz \right]^2}. \quad (11)$$

Figure 12 shows models of the predicted amplitude of  $\omega(\theta)$  as a function of magnitude for different values of  $x_0(0)$  and  $\epsilon$ , given our fits for  $dN/dz$ . An increase in  $x_0(0)$  has the effect of shifting the predicted values higher, increasing the amplitude of clustering at all magnitudes, while increasing  $\epsilon$  creates a steeper slope in the evolution of clustering. We find that our data is not well-fit by any single value of  $\epsilon$ ; the brightest galaxies are best-fit by  $\epsilon \sim 0$  and  $x_0(0) \sim 5 \ h^{-1}$  Mpc, to  $I_{AB} \sim 21$ . The amplitude of  $\omega(\theta)$  at  $1'$  then begins to decrease more rapidly than an  $\epsilon = 0$  model predicts, such that the fainter galaxies imply a value of  $\epsilon \sim 3$ . This implies significant growth of clustering at intermediate redshifts ( $z \sim 0.5 - 1$ ) and clustering fixed in physical coordinates in the more recent past ( $z \sim 0 - 0.5$ ). A model with  $\epsilon \sim 3$  does not match our data within the errors across the full magnitude range; in particular, the model predictions are low for  $I_{AB} \sim 20 - 23$ . The  $\epsilon$  model is known

not to fit angular clustering data well (McCracken et al. 2001; Wilson 2003) and is in fact not a physically realistic model given the presence of a galaxy bias which evolves with redshift. Therefore we attempt to find a new model which better fits the data.

Given that  $\omega(\theta)$  declines monotonically with the median  $I_{AB}$  magnitude of a sample, and that  $z_0$  is well-fit as a linear function of the median  $I_{AB}$  magnitude, we propose a linear model for the evolution of  $x_0(z)$ ,  $x_0(z) = x_0(0)(1 - Bz)$ . We stress that this linear model for the evolution of  $x_0(z)$  is valid only in the redshift range this dataset is sensitive to, namely  $z \sim 0 - 1.5$ , and  $x_0$  is expected to increase at higher redshifts, as seen in both data and simulations (e.g., Adelberger et al. 2003; Kauffmann et al. 1999). For this model,  $\xi(r)$  evolves as

$$\xi(x, z) = \left[ \frac{x_0(z)}{x} \right]^\gamma = \left[ \frac{x_0(0)(1 - Bz)}{x} \right]^\gamma = \xi(x, 0)(1 - Bz)^\gamma. \quad (12)$$

Replacing the  $x_0(z)$  term in Equation 6 with  $x_0(0)(1 - Bz)$ , we can fit for  $B$  and  $x_0(0)$ . Fits for the linear model are shown in Figure 13; the best fit is  $x_0(0) \sim 5 - 6 \ h^{-1}$  Mpc and  $B \sim 0.6 - 0.9$ . These values imply that  $x_0(z = 0.8) \sim 1.4 - 3.1 \ h^{-1}$  Mpc and  $x_0(z = 1.1) \sim 0.1 - 2.0 \ h^{-1}$  Mpc.  $\xi(r)$  results from early DEEP2 data measure  $x_0(z = 0.8) = 3.5 \pm 0.8 \ h^{-1}$  Mpc and  $x_0(z = 1.1) = 3.1 \pm 0.7 \ h^{-1}$  Mpc (Coil et al. 2004), somewhat higher than what is implied here, though within  $1-2-\sigma$  of the upper range of values.

We do not necessarily expect the results to match exactly, as the  $\xi(r)$  results are for a data sample with a limiting magnitude of  $R_{AB} = 24.1$ , which is roughly half a magnitude brighter than our faintest  $\omega(\theta)$  sample. Additionally, a luminosity-dependent bias, which is expected to exist at  $z \simeq 1$  (e.g., Coil et al. 2004; Kauffmann et al. 1999), would cause the  $\omega(\theta)$  results from our faintest magnitude bin to imply a somewhat lower value of  $x_0(z)$ . There are other possible factors that may contribute to this discrepancy; a wider  $dN/dz$  distribution, especially at the higher redshifts, would imply larger values of  $x_0(z)$ , though comparisons to other surveys do not indicate that our redshift distributions are too narrow. Limber’s equation also has implicit assumptions which may break down at some level; for example, Limber’s equation holds that the probability of finding a galaxy pair at a given separation depends on  $\xi(r)$  multiplied by the selection function for each galaxy. This implies that galaxies have a selection function which is independent of their clustering. This assumption does not hold if clustering depends on environment or luminosity, for example, which is known to be true both locally and at intermediate redshifts. This may affect our ability to interpret  $\omega(\theta)$  results when using a sample that includes a mix of galaxy types, luminosities and redshifts.

## 6. GALAXY CLUSTERING AS A FUNCTION OF $(R - I)$ COLOR

We now parallel the previous section, discussing the clustering as a function of color instead of magnitude. We plot in Figure 14 the amplitude of  $\omega(\theta)$  at  $1'$  for nine independent  $(R - I)$  color bins, where we fit for the slope and amplitude simultaneously. Each bin has a width of  $(R - I) = 0.2$ , and we use all galaxies in the magnitude range  $I_{AB} = 18 - 24$ . Table 5 lists the computed

amplitude and errors of  $\omega(\theta)$  measured at  $1'$  for each color range. Similar to  $\omega(\theta)$  as a function of magnitude (Section 5.2), we find that the results are consistent if we first sum the DD, DR, and RR pairs across all the pointings before taking the ratio in Equation (2) and errors are estimated using bootstrap resampling of the data. There is a strong, monotonic progression between  $0.2 < (R - I) < 1.5$  of redder galaxies having a higher clustering strength. This trend is not surprising, as red galaxies have long been known to be more strongly clustered than blue galaxies locally and this trend appears to continue to  $z \simeq 1$  (recent results include Willmer et al. 1998, Zehavi et al. 2002, Coil et al. 2003). We also find that there is a sharp rise in the clustering amplitude for the bluest galaxies in our sample ( $-0.2 < (R - I) < 0.0$ ), which have a clustering strength comparable to the reddest galaxies ( $1.2 < (R - I) < 1.6$ ). Landy, Szalay, & Koo (1996) first reported such a marked correlation of clustering with color, in a sample of  $\sim 3000$  galaxies selected by  $U - R_F$  color, where they found that the bluest and reddest galaxies showed much strong clustering than the sample as a whole. More recently, with larger surveys, McCracken et al. (2001) and Wilson (2003) also find similar clustering trends with  $V - I$  color and report that the bluest and reddest samples are highly clustered. We note that the strong rise in clustering amplitude seen for the bluest galaxies is only apparent after rather stringent color cuts are made ( $R - I < 0.2$ ), and that galaxies which are selected to be blue based on a  $B$  magnitude alone do not show strong clustering (e.g., Efstathiou et al. 1991).

Figure 15 shows the best-fit slope for each color bin, as listed in Table 5. We find that galaxies with  $0.2 < (R - I) < 1.0$  have slopes of  $-0.6 \lesssim \delta \lesssim -0.8$ , while the bluest and reddest samples have steeper slopes, with  $-1.0 \lesssim \delta \lesssim -1.4$ . This implies that the slope of  $\xi(r)$  for the bluer and redder samples is steeper than for galaxies with  $0.2 < (R - I) < 1.0$ . Locally, the slope of  $\xi(r)$  in SDSS galaxies is found to be  $\gamma = 1.86 \pm 0.03$  for redder galaxies with a restframe color of  $u^* - r^* > 1.8$  and  $\gamma = 1.41 \pm 0.04$  for bluer galaxies with  $u^* - r^* < 1.8$  (Zehavi et al. 2002). At intermediate redshifts ( $0.1 < z < 0.5$ ) Shepherd et al. (2001) find that galaxies with early-type SEDs have a clustering slope of  $\gamma = 1.91 \pm 0.06$  while late-type galaxies show  $\gamma = 1.59 \pm 0.08$ . Our results imply a slope of  $\gamma \gtrsim 2.0$  for the reddest galaxies, and  $\gamma \sim 1.6 - 1.7$  for typical blue galaxies. The very bluest galaxies, with  $(R - I) < 0$ , appear not to be typical intermediate-redshift blue galaxies, as described in the following sections.

### 6.1. Redshift Distributions of Different Color Ranges

Using the sample of 2954 early DEEP2 galaxies with secure redshifts between  $0 < z < 1.5$  in the EGS we construct redshift distributions for sources as a function of  $(R - I)$  color as shown by the solid lines in Figure 16. Note that these histograms do not have the same scale on the y-axis, as the number of galaxies in each bin varies widely. The reddest galaxies, with  $1.2 < (R - I) < 1.6$ , lie in a relatively narrow redshift range centered near  $z \sim 0.85$ . Successively bluer bins have both a lower median redshift and a wider redshift distribution. Galaxies with  $0.0 < (R - I) < 0.4$  appear to be predominately centered at  $z \sim 0.35$ , though there is a tail to higher

redshifts. The bluest galaxies ( $-0.2 < (R - I) < 0.0$ ) have a narrow redshift distribution between  $z \sim 0 - 0.5$ . As discussed above, the DEEP2 Redshift Survey can not measure redshifts for galaxies at  $z \gtrsim 1.45$  as observable emission and absorption line features move out of the spectral wavelength range of our data. These redshift histograms are therefore missing galaxies at  $z \gtrsim 1.45$ . The redshift success rate of the DEEP2 survey in the EGS is fairly insensitive to color in the range  $0.2 < (R - I) < 1.6$ , where the success rate is  $\geq 80\%$  and where 90% of the targeted objects lie, but it begins to drop blueward of  $(R - I) \sim 0.2$ . For galaxies with  $0.0 < (R - I) < 0.2$  the redshift success rate is  $\sim 55\%$ , while the bluest galaxies, with  $-0.2 < (R - I) < 0.0$ , have a success rate of  $\sim 30\%$ . We believe that most of the observed galaxies without redshifts lie at  $z > 1.45$ , as these blue galaxies should have emission lines which we would detect at lower redshifts. The sample of 20 DEEP2 blue galaxies without measured redshifts which Chuck Steidel has followed were all found to lie at  $z > 1.45$  (see Section 5.4 for details). We therefore correct the bluest two redshift distributions by assigning redshifts to the galaxies without measured redshifts such that they have a Gaussian distribution with a mean of  $z = 1.75$  and a standard deviation of  $\sigma = 0.30$ , matching the distribution of sources followed by Steidel. These corrected redshift distributions can be seen in Figure 16 as the dashed lines for the two bluest distributions.

### 6.2. Clustering Scale-length as a Function of $(R - I)$ Color

Figure 17 shows the comoving scale-length  $x_0$  as a function of  $(R - I)$  color calculated using the observed redshift distributions shown in Figure 16 in solid lines, assuming that  $x_0$  is constant over the redshift range of galaxies in each color bin. The errors on  $x_0$  are derived from the errors on  $\omega(\theta)$  alone and do not include uncertainties in the redshift distribution; therefore they may be underestimates of the true error. Values of  $x_0$  and associated errors are given in Table 5. As dividing the galaxies into color bins results in more uniform populations within a single bin, we believe that Limber's equation should be more robust in interpreting  $\omega(\theta)$  as a function of color.

For the reddest galaxies, with  $1.4 < (R - I) < 1.6$ , we find  $x_0 = 5.02 \pm 0.26 h^{-1}$  Mpc (note that this is the comoving scale-length at the redshift of the sample). These galaxies, centered at  $z \sim 0.85$ , have absorption-dominated spectra and are likely to be massive progenitors of local ellipticals. Our value is somewhat lower than that found by Brown et al. (2003), who measure early-type galaxies with  $B_W - R > 1.28$  between  $0.7 < z < 0.9$  to have  $x_0 = 6.6 \pm 0.8 h^{-1}$  Mpc. Locally, Budavari et al. (2003) finds from an angular clustering study of SDSS galaxies that  $x_0(0) = 6.59 \pm 0.17 h^{-1}$  Mpc and  $\delta = -0.96 \pm 0.05$  for early-type galaxies with  $-21 > M_r > -23$ . Our results at  $z \sim 0.85$  are consistent with predictions of little evolution of  $x_0(z)$  for early-type galaxies from  $z \sim 1$  to 0 (Kauffmann et al. 1999; Benson et al. 2001). Our reddest sample may be a less-extreme version of the extremely red object (ERO) population which are seen to have large clustering at  $z \sim 1$  with  $x_0 \sim 7.5 - 12 h^{-1}$  Mpc (e.g., Daddi et al. 2001; Firth et al. 2002).

The comoving scale-length decreases as galaxies be-

come bluer to a minimum of  $x_0 = 1.60 \pm 0.23 \ h^{-1} \text{ Mpc}$  at  $0.2 < (R - I) < 0.4$ . These galaxies lie predominantly between  $z \sim 0.3 - 0.6$ , though there is a small tail at  $z > 1.0$ . The redshift distribution of galaxies with  $0.0 < (R - I) < 0.2$  is strongly bimodal; this sample appears to be a mix of two populations: relatively local galaxies similar to the sample with  $0.2 < (R - I) < 0.4$  and a  $z > 1.4$  population of bright, star-forming galaxies. If the angular clustering is due entirely to the lower-redshift population, then  $x_0 = 2.47 \pm 0.32 \ h^{-1} \text{ Mpc}$ , where we have used the uncorrected redshift distribution shown as a solid line in Figure 16. If the clustering is due entirely to the higher-redshift population, then  $x_0 = 3.8 \ h^{-1} \text{ Mpc}$ . More likely, however, is that the observed  $\omega(\theta)$  value is a mixture of these two populations, and we would like to separate their contributions to  $\omega(\theta)$  and measure values of  $x_0$  for each population, as they may have different intrinsic clustering properties. It can be shown that  $\omega(\theta)$  from a combined sample of disparate populations with different clustering properties and non-overlapping  $dN/dz$  distributions adds linearly such that

$$\omega(\theta)_{\text{total}} = f_1^2 \omega_1(\theta) + (1 - f_1)^2 \omega_2(\theta) \quad (13)$$

where  $f_1$  is the fraction of the total number of galaxies in one population,  $(1 - f_1)$  is the fraction in the other population, and  $\omega_1(\theta)$  and  $\omega_2(\theta)$  are the angular clustering amplitudes of each population (e.g., Meiksin, White, & Peacock 1999). The value of  $x_0 = 3.8 \ h^{-1} \text{ Mpc}$  which we find for the  $z > 1.4$  population is therefore a lower limit on the clustering scale-length of that population, as some of the observed projected clustering is due to the lower-redshift sample. If we use the value of  $\omega(\theta)$  observed for the  $0.2 < (R - I) < 0.4$  sample as the clustering contribution from the lower-redshift population, we can then subtract this from the observed  $\omega(\theta)$  amplitude for the  $0.0 < (R - I) < 0.2$  sample, assuming that  $\sim 50\%$ - $75\%$  of the galaxies in this color bin are in the lower-redshift population. Using the redshift distribution of the  $z > 1.4$  galaxies shown in Figure 16, we find  $x_0 = 7.8 \pm 0.3 \ h^{-1} \text{ Mpc}$  for the  $z > 1.4$  galaxies if 50% of the galaxies in this color bin are in this population (corresponding to all the galaxies without measured redshifts), and  $x_0 = 5.2 \pm 0.4 \ h^{-1} \text{ Mpc}$  if 25% of the galaxies are at  $z > 1.4$  (corresponding to half of the galaxies without measured redshifts). These values most likely bracket the true value, as the percentage of galaxies without measured redshifts at  $z > 1.4$  is likely to be between 50%-100%. These results are shown in Figure 17. It is worth noting that this error does not include uncertainties in the redshift distribution of  $z > 1.4$  galaxies.

In the bluest color bin,  $-0.2 < (R - I) < 0.0$ , the number of galaxies drops dramatically and the redshift distribution for objects at  $z < 1.4$  appears to be relatively narrow, though the robustness of this width is uncertain given the small sample size. If the clustering of the bluest objects is due to galaxies with the uncorrected redshift distribution shown as a solid line in the upper left panel of Figure 16, then  $x_0 = 3.69 \pm 0.87 \ h^{-1} \text{ Mpc}$ . However, as the redshift success rate is only  $\sim 30\%$  for galaxies in this bin in the DEEP2 EGS region, it is likely that most of the objects in this color range are at  $z > 1.4$ , since they must be actively forming stars to have such blue colors and would therefore have strong nebular emission lines which would allow DEEP2 to determine their redshifts

easily if at  $z < 1.4$ . A third population also contributes to objects found in this color bin: broad-line AGN found in the DEEP2 sample disproportionately have  $(R - I) < 0$ . In the EGS, where the photometric-redshift pre-selection of targets is not applied, 11% of the galaxies in the bluest bin are identified as broad-line AGN, whereas  $\lesssim 1\%$  are objects with  $(R - I) > 0$  are so classified. These percentages are lower limits, since the spectroscopic signatures of weak AGN could be dominated by galaxy light and therefore remain undetected. The AGN identified in DEEP2 spectra span the full redshift range  $0 < z < 1.5$ . The bluest color bin,  $-0.2 < (R - I) < 0.0$ , thus includes at least three distinct populations: faint blue galaxies at low redshift, bright star-forming galaxies at  $z > 1.4$ , and broad-line AGN with strong, blue continua.

Separating the contributions to the observed total  $\omega(\theta)$  from each population is not entirely straightforward, as there are uncertainties in both the estimates of the fraction of objects in each population and their redshift distributions. However, given the small percentage of local galaxies seen in the observed redshifts for this bin and the low clustering amplitude of the local star-forming galaxies in the  $0.2 < (R - I) < 0.4$  bin, which have  $x_0 = 1.60 \pm 0.23 \ h^{-1} \text{ Mpc}$ , it seems unlikely that local galaxies alone account for the large clustering signal seen here. A sample of local galaxies with the same relatively redshift distribution and clustering scale-length as those in the  $0.2 < (R - I) < 0.4$  color range, would have a  $\omega(\theta)$  value 13% as large as what is measured in this bin, in opposition to the conclusions of Landy, Szalay, & Koo (1996), McCracken et al. (2001) and Wilson (2003), who suggest that the strong clustering of blue galaxies is dominated by a local galaxy population.

If the observed  $\omega(\theta)$  in this color bin was due entirely to  $z > 1.4$  galaxies, the clustering scale-length for that population would be  $x_0 = 7.5 \pm 1.5 \ h^{-1} \text{ Mpc}$ . If AGN were the sole contributing population and had the same redshift distribution as the local galaxies in this color bin, they would have a clustering scale-length of  $x_0 = 3.69 \pm 0.87 \ h^{-1} \text{ Mpc}$ , the same as for local galaxies. Observations of AGN and QSO clustering have found scale-lengths comparable to local early-type galaxies, with  $x_0 \sim 6 - 8 \ h^{-1} \text{ Mpc}$ , and very little evolution in the scale-length with redshift (Croom et al. 2002; Grazian et al. 2004). It therefore seems quite feasible that AGN contribute significantly to the large clustering seen in this color range. Assuming that the observed  $\omega(\theta)$  is due to a combination of these three populations, and that each of them is totally independent, would lead to much larger values for  $x_0$  of each subsample, possibly in excess of other estimates of the clustering of  $z > 1.4$  galaxies and AGN. It is likely that not only the autocorrelation of each population, but also its cross-correlation with the other sets of extremely blue objects, leads to the strong observed clustering in this color bin.

In order to check the degree of independence between the redshift distributions in each sample, we measure the cross-correlation between galaxies in color bins  $i$  and  $j$ ,  $w_{ij}(\theta)$ , and normalize each correlation amplitude,  $A_{w_{ij}}$ , by the square root of the auto-correlation function amplitude,  $A_{w_{ii}}$ :

$$c_{ij} = \frac{A_{w_{ij}}(1')}{\sqrt{A_{w_{ii}}(1')A_{w_{jj}}(1')}} \quad (14)$$

where we have measured  $w(1')$  assuming a constant slope of  $\delta = -0.8$  and  $w_{ij}$  is defined by equation 3 where DD is replaced with  $D_i D_j$ . This results in a covariance matrix, shown in Table 6, that provides information on the physical covariance between galaxies in each color bin. Our results are generally consistent with the covariance of the redshift distributions seen in Figure 16. Each color sample shows significant covariance with the immediately adjacent samples, and galaxies in the reddest four color bins, with  $0.8 < (R - I) < 1.6$ , all have significant covariance with each other. The bluest color bin does not have significant covariance with galaxies with  $0.2 < (R - I) < 0.4$ , implying that the relatively local, blue, star-forming galaxies with low correlation seen in the  $0.2 < (R - I) < 0.4$  range contribute very little to the clustering seen in the bluest population, as we assumed above. However, the  $z > 1.4$  galaxy population must contribute to both of the bluest two color bins. This covariance matrix provides a reassuring check on our redshift distributions used to interpret  $\omega(\theta)$  as a function of color.

## 7. SUMMARY AND CONCLUSIONS

We measure the projected angular correlation function,  $\omega(\theta)$ , using deep photometric imaging with a sample of 350,000 galaxies to  $I_{AB} = 24$ , a significant subset of which is used as photometric data for the DEEP2 Galaxy Redshift Survey. Our data covers a total of 5 degrees<sup>2</sup> over 5 separate fields, a larger area than has been studied by previous deep angular clustering surveys. This increase in area, combined with galaxy redshift distributions derived from a relatively large, uniform spectroscopic sample of 2954 DEEP2 galaxies between  $0 < z < 2$ , leads to tighter constraints on models than has been previously available. Using robust redshift distributions as a function of color also allows for quantitative interpretations of the strong trends seen in  $\omega(\theta)$  vs. observed  $(R - I)$ .

We find that there has been significant growth of clustering from  $z > 1$  to  $z \sim 0$ , and that the ‘ $\epsilon$ -model’ proposed by Groth & Peebles (1977) does not describe the evolution of clustering well. We propose an alternative

model in which the comoving scale-length,  $x_0(z)$ , evolves linearly over the redshift range we are sensitive to here and find that this model better describes the data. We find that  $x_0 \sim 1 - 3 h^{-1}$  Mpc at  $z \sim 1$ , though these results are not straightforward to interpret, as they result not only from intrinsic evolution, but also any changes in the mean luminosity, color, and type of galaxies with redshift.

We also find that  $\omega(\theta)$  is a very sensitive function of observed  $(R - I)$  color, with both the reddest and bluest galaxies showing strong clustering amplitudes and steeper clustering slopes. Red galaxies with  $1.4 < (R - I) < 1.6$  have a comoving scale-length of  $x_0 = 5.02 \pm 0.26 h^{-1}$  Mpc and lie in a narrow redshift range centered at  $z \sim 0.85$ . Their spectra indicate that these galaxies have older stellar populations and are likely to be progenitors of local ellipticals. The clustering amplitude decreases with color to a minimum at  $0.2 < (R - I) < 0.4$ , where  $x_0 = 1.60 \pm 0.23 h^{-1}$  Mpc for blue star-forming galaxies between  $z \sim 0.3 - 0.6$ . The bluest galaxies, with  $(R - I) < 0$ , are very highly clustered, and include additional populations of  $z > 1.4$  bright, star-forming galaxies with a scale-length of  $x_0 \gtrsim 5 h^{-1}$  Mpc and broad-line AGN. We find that the clustering of the bluest galaxies is not likely to be dominated by a local population or due entirely to high-redshift galaxies.

We thank Chuck Steidel, Jim Peebles and David Hogg for useful discussions. We also thank the DEEP2 team for generously providing early redshift data and Andy Connolly for his vital work on obtaining photometric calibrations for the DEEP2 fields. An anonymous referee provided insightful and constructive comments. This project was supported by the NSF grant AST-0071048. J.A.N. acknowledges support by NASA through Hubble Fellowship grant HST-HF-01165.01-A awarded by the Space Telescope Science Institute, which is operated by AURA Inc. under NASA contract NAS 5-26555. C.-P. M. is partially supported by a Cottrell Scholars Award from the Research Corporation and NASA grant NAG5-12173.

## REFERENCES

- Adelberger, K. L., et al. 2003, *ApJ*, 584, 45  
 Arnouts, S., et al. 1999, *A&A*, 341, 641  
 Benson, A. J., et al. 2001, *MNRAS*, 327, 1041  
 Brainerd, T. G., Smail, I., & Mould, J. 1995, *MNRAS*, 275, 781  
 Brodwin, M., et al. 2003, submitted to *ApJ* (astro-ph/0310038)  
 Brown, M. J. I., et al. 2003, *ApJ*, 597, 225  
 Brunner, R. J., Connolly, A. J., & Szalay, A. S. 1999, *ApJ*, 516, 563  
 Budavari, T., et al. 2003, *ApJ*, 595, 59  
 Cabanac, R. A., de Lapparent, V., & Hickson, P. 2000, *A&A*, 364, 349  
 Charlot, S., Worthey, G., & Bressan, A. 1996, *ApJ*, 457, 625  
 Coil, A. L., et al. 2004, accepted by *ApJ* (astro-ph/0305586)  
 Cowie, L. L., Songaila, A., & Barger, A. J. 1999, *AJ*, 118, 603  
 Croom, S. M., et al. 2002, *MNRAS*, 335, 459  
 Daddi, E., et al. 2001, *A&A*, 376, 825  
 Davis, M., et al. 2002, *Proc. SPIE*, 4834, 161 (astro-ph 0209419)  
 Efsthathiou, G., Bernstein, G., Tyson, J. A., Katz, N., & Guhathakurta, P. 1991, *ApJ*, 380, L47  
 Fioc, M., & Rocca-Volmerange, B. 1997, *A&A*, 326, 950  
 Firsh, A. E., et al. 2002, *MNRAS*, 332, 617  
 Grazian, A., Negrello, M., Moscardini, L., Cristiani, S., Haehnelt, M. G., Matarrese, S., Omizzolo, A., & Vanzella, E. 2004, *AJ*, 127, 592  
 Groth, E. J., & Peebles, P. J. E. 1977, *ApJ*, 217, 385  
 Hogg, D. W., et al. 1997, *MNRAS*, 288, 404  
 Hudon, J. D., & Lilly, S. J. 1996, *ApJ*, 469, 519  
 Jannuzi, B. T., & Dey, A. 1999, In *ASP Conf. Ser. 191: Photometric Redshifts and the Detection of High Redshift Galaxies*, p. 111  
 Kauffmann, G., Colberg, J. M., Diaferio, A., & White, S. D. M. 1999, *MNRAS*, 307, 529  
 Kerscher, M., Szapudi, I., & Szalay, A. S. 2000, *ApJ*, 535, L13  
 Landy, S. D., & Szalay, A. S. 1993, *ApJ*, 412, 64  
 Landy, S. D., Szalay, A. S., & Koo, D. C. 1996, *ApJ*, 460, 94  
 Madgwick, D. S., et al. 2003, *ApJ*, 599, 997  
 McCracken, H. J., et al. 2000, *MNRAS*, 318, 913  
 McCracken, H. J., et al. 2001, *A&A*, 376, 756  
 McCracken, H. J., et al. 2003, *A&A*, 410, 17  
 Meiksin, A., White, M., & Peacock, J. A. 1999, *MNRAS*, 304, 851  
 Metcalfe, N., et al. 2001, *MNRAS*, 323, 795  
 Neuschaefer, L. W., & Windhorst, R. A. 1995, *ApJ*, 439, 14  
 Newman, J., et al. 2004, in preparation  
 Norberg, P., et al. 2001, *MNRAS*, 328, 64  
 Peebles, P. J. E. 1975, *ApJ*, 196, 647  
 Peebles, P. J. E. 1980. *The Large-Scale Structure of the Universe*, Princeton, N.J., Princeton Univ. Press  
 Postman, M., Lauer, T. R., Szapudi, I., & Oegerle, W. 1998, *ApJ*, 506, 33

TABLE 1. DETAILS OF OUR CFHT12K OBSERVATIONS.

Field	pointing	RA	Dec.	exp. time (hrs)			seeing (FWHM)	date of obs.
				B	R	I		
0230	1	02 27 30	00 35 00	1.0	1.0	2.2	0.8 "	10-11/99 09/00
	2	02 30 00	00 35 00	0.7	1.0	2.0	0.7 "	10-11/99 09/00
	3	02 32 30	00 35 00	0.8	1.0	2.0	0.7 "	10-11/99 09/00
1052	1	10 52 43	56 58 48	1.0	1.5	1.0	0.69 "	04/01
1416	1	14 15 29	52 08 19	1.0	1.0	1.0	0.9 "	05/00 04/01
	2	14 17 55	52 35 07	1.8	1.0	1.3	1.0 "	05/00 04-05/01
	3	14 20 21	53 01 55	1.2	1.5	2.0	0.7 "	05/00 04-05-07/01
1651	1	16 48 00	34 55 02	1.7	2.5	1.0	0.9 "	05-09-10/00 05/01
	2	16 51 30	34 55 02	1.8	1.0	1.0	0.9 "	05-09/00 04-05/01
	4	16 55 28	33 42 00	1.0	1.8	1.7	0.8 "	05-09-10/00
2330	1	23 26 56	00 08 00	1.3	1.0	3.3	0.8 "	10-11/99 09/00
	2	23 30 00	00 08 00	1.0	1.0	3.0	0.8 "	10-11/99 09/00
	3	23 33 03	00 08 00	1.0	1.0	2.0	0.7 "	10-11/99 09/00
	4	23 25 40	00 -40 00	0.8	1.0	0.5	0.8 "	10/99 09/00
	5	23 34 00	00 50 00	1.2	1.0	1.0	0.8 "	10/99 09-10/00

TABLE 2. POWER LAW FITS TO  $\omega(\theta) = A_\omega \theta^\delta$  AS A FUNCTION OF  $I_{AB}$  MAGNITUDE.

$I_{AB}$ range	median $I_{AB}$	# gals/pt.	$A_\omega(1')$ ( $\delta = -0.8$ )	$A_\omega(1')$	$\delta$
18 – 19	18.6	152	$0.187 \pm 0.023$	$0.184 \pm 0.027$	$-0.82 \pm 0.10$
19 – 20	19.6	453	$0.070 \pm 0.010$	$0.067 \pm 0.010$	$-1.01 \pm 0.09$
20 – 21	20.6	1224	$0.060 \pm 0.004$	$0.045 \pm 0.005$	$-0.99 \pm 0.05$
21 – 22	21.6	2812	$0.031 \pm 0.001$	$0.027 \pm 0.002$	$-0.90 \pm 0.04$
22 – 23	22.6	5921	$0.015 \pm 0.001$	$0.017 \pm 0.001$	$-0.74 \pm 0.05$
23 – 24	23.6	11879	$0.007 \pm 0.001$	$0.008 \pm 0.001$	$-0.70 \pm 0.07$

TABLE 3. FITS FOR THE REDSHIFT DISTRIBUTION OF DEEP2 SPECTROSCOPIC SOURCES AS A FUNCTION OF MAGNITUDE, FOR DIFFERENTIAL MAGNITUDE BINS, ASSUMING  $dN/dz \propto z^2 \exp(-z/z_0)$ . THE CORRECTED VALUES OF  $z_0$  INCLUDE GALAXIES AT  $z > 1.4$  (SEE TEXT FOR DETAILS).

$I_{AB}$ range	uncorrected $z_0$	corrected $z_0$	$z_0$ error
18 - 19	0.091	0.091	0.010
19 - 20	0.136	0.136	0.007
20 - 21	0.197	0.197	0.005
21 - 22	0.237	0.239	0.005
22 - 23	0.278	0.288	0.006
23 - 24	0.285	0.324	0.010

Roche, N., & Eales, S. A. 1999, MNRAS, 307, 703  
 Roche, N., Shanks, T., Metcalfe, N., & Fong, R. 1993, MNRAS, 263, 360  
 Shepherd, C. W., et al. 2001, ApJ, 560, 72  
 Steidel, C. C., Shapley, A. E., Pettini, M., Adelberger, K. L., Erb, D. K., Reddy, N. A., & Hunt, M. P. 2004, ApJ, 604, 534  
 Willmer, C. N. A., da Costa, L. N., & Pellegrini, P. S. 1998, AJ, 115, 869

Wilson, G. 2003, ApJ, 585, 191–204  
 Woods, D., & Fahlman, G. G. 1997, ApJ, 490, 11  
 York, D. G., et al. 2000, AJ, 120, 1579  
 Zehavi, I., et al. 2002, ApJ, 571, 172

TABLE 4. FITS FOR THE REDSHIFT DISTRIBUTION OF DEEP2 SPECTROSCOPIC SOURCES AS A FUNCTION OF MAGNITUDE, FOR INTEGRAL MAGNITUDE BINS.

$R_{AB}$ range	$z_0^a$	$z_0^b$	$I_{AB}$ range	$z_0^a$	$z_0^b$
18 - 20	0.104	0.145	18 - 20	0.123	0.171
18 - 21	0.136	0.188	18 - 21	0.168	0.232
18 - 22	0.168	0.232	18 - 22	0.206	0.284
18 - 23	0.207	0.285	18 - 23	0.242	0.332
18 - 24	0.255	0.350	18 - 24 <sup>c</sup>	0.283	0.389
18 - 25 <sup>c</sup>	0.286	0.392	18 - 25 <sup>c</sup>	0.322	0.443
18 - 26 <sup>c</sup>	0.324	0.443	18 - 26 <sup>c</sup>	0.362	0.496
18 - 27 <sup>c</sup>	0.361	0.494	18 - 27 <sup>c</sup>	0.401	0.550

<sup>a</sup>for  $dN/dz \propto z^2 \exp(-z/z_0)$

<sup>b</sup>for  $dN/dz \propto z^2 \exp(-z/z_0)^{1.2}$

<sup>c</sup>extrapolated using a linear fit (see text for details)

TABLE 5. POWER LAW FITS TO  $\omega(\theta) = A_\omega \theta^\delta$  AS A FUNCTION OF  $(R - I)$  COLOR, USING THE OBSERVED REDSHIFT HISTOGRAMS SHOWN IN FIGURE 16 (SOLID LINES).

$(R - I)$ range	median $(R - I)$	# gals/pt	$A_\omega(1')$ ( $\delta = -0.8$ )	$A_\omega(1')$	$\delta$	$x_0(z)$ Mpc $h^{-1}$
-0.2 - 0.0	-0.05	274	$0.118 \pm 0.021$	$0.113 \pm 0.023$	$-1.36 \pm 0.21$	$3.69 \pm 0.87$
0.0 - 0.2	0.14	1869	$0.037 \pm 0.003$	$0.041 \pm 0.005$	$-0.69 \pm 0.11$	$2.47 \pm 0.32$
0.2 - 0.4	0.31	5796	$0.012 \pm 0.001$	$0.014 \pm 0.001$	$-0.59 \pm 0.08$	$1.60 \pm 0.23$
0.4 - 0.6	0.50	5745	$0.019 \pm 0.001$	$0.021 \pm 0.001$	$-0.69 \pm 0.06$	$2.78 \pm 0.36$
0.6 - 0.8	0.69	4415	$0.031 \pm 0.001$	$0.032 \pm 0.002$	$-0.78 \pm 0.05$	$3.34 \pm 0.30$
0.8 - 1.0	0.88	2364	$0.048 \pm 0.003$	$0.049 \pm 0.003$	$-0.76 \pm 0.07$	$3.38 \pm 0.22$
1.0 - 1.2	1.09	1221	$0.080 \pm 0.005$	$0.072 \pm 0.006$	$-1.02 \pm 0.07$	$4.18 \pm 0.22$
1.2 - 1.4	1.29	861	$0.098 \pm 0.006$	$0.093 \pm 0.006$	$-1.25 \pm 0.06$	$4.25 \pm 0.33$
1.4 - 1.6	1.46	308	$0.171 \pm 0.014$	$0.144 \pm 0.016$	$-1.14 \pm 0.10$	$5.02 \pm 0.26$

TABLE 6. COVARIANCE OF  $\omega(\theta)$  AS A FUNCTION OF  $(R - I)$  COLOR

$(R - I)$ range	-0.2-0.0	0.0-0.2	0.2-0.4	0.4-0.6	0.6-0.8	0.8-1.0	1.0-1.2	1.2-1.4	1.4-1.6
-0.2-0.0	1.00	0.66	0.14	-0.06	-0.22	-0.19	-0.06	-0.14	-0.36
0.0-0.2	0.66	1.00	0.62	0.12	-0.13	-0.16	-0.19	-0.20	-0.26
0.2-0.4	0.14	0.62	1.00	0.64	0.26	0.09	-0.06	-0.01	-0.02
0.4-0.6	-0.06	0.12	0.64	1.00	0.70	0.38	0.22	0.25	0.10
0.6-0.8	-0.22	-0.13	0.26	0.70	1.00	0.72	0.57	0.63	0.43
0.8-1.0	-0.19	-0.16	0.09	0.38	0.72	1.00	0.87	0.71	0.49
1.0-1.2	-0.06	-0.19	-0.06	0.22	0.57	0.87	1.00	0.92	0.54
1.2-1.4	-0.14	-0.20	-0.01	0.25	0.63	0.71	0.92	1.00	0.81
1.4-1.6	-0.36	-0.26	-0.02	0.10	0.43	0.49	0.54	0.81	1.00

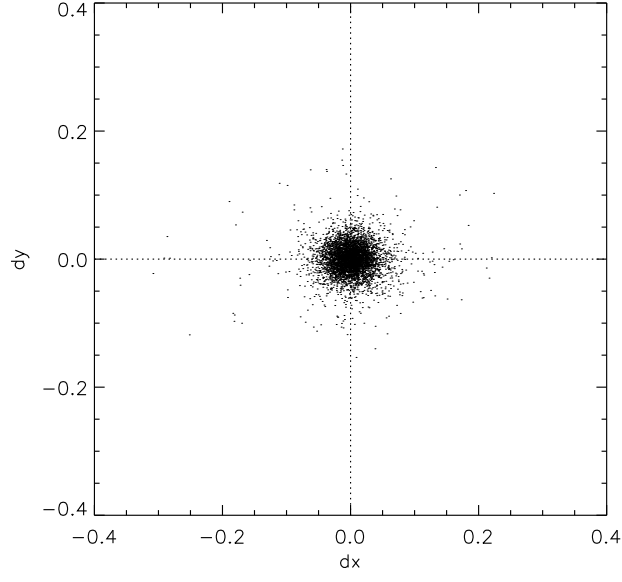


FIG. 1.— Residuals in the astrometric solution, with units in pixels. The rms is  $\sim 0.025$  pixels, corresponding to  $\sim 0.005''$ .

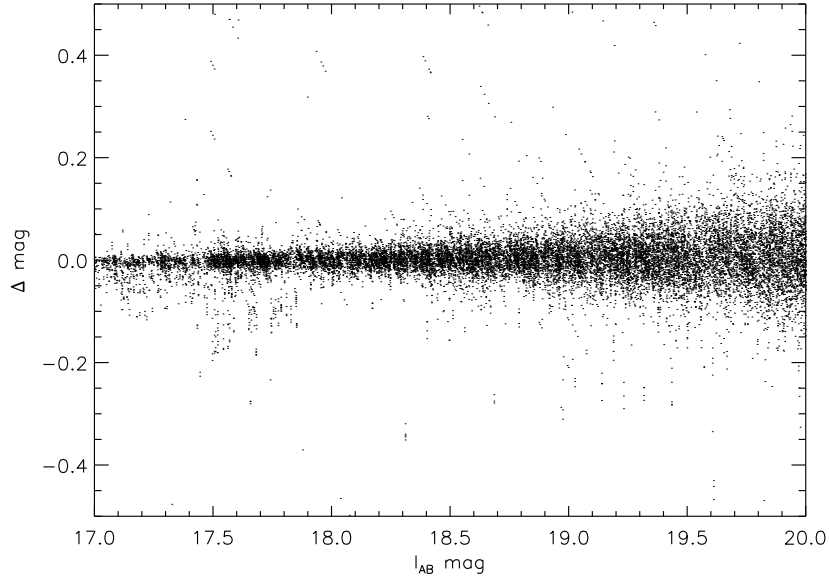


FIG. 2.— Differences in magnitudes for stars detected on multiple exposures. The rms at bright magnitudes is  $\sim 0.02$ .

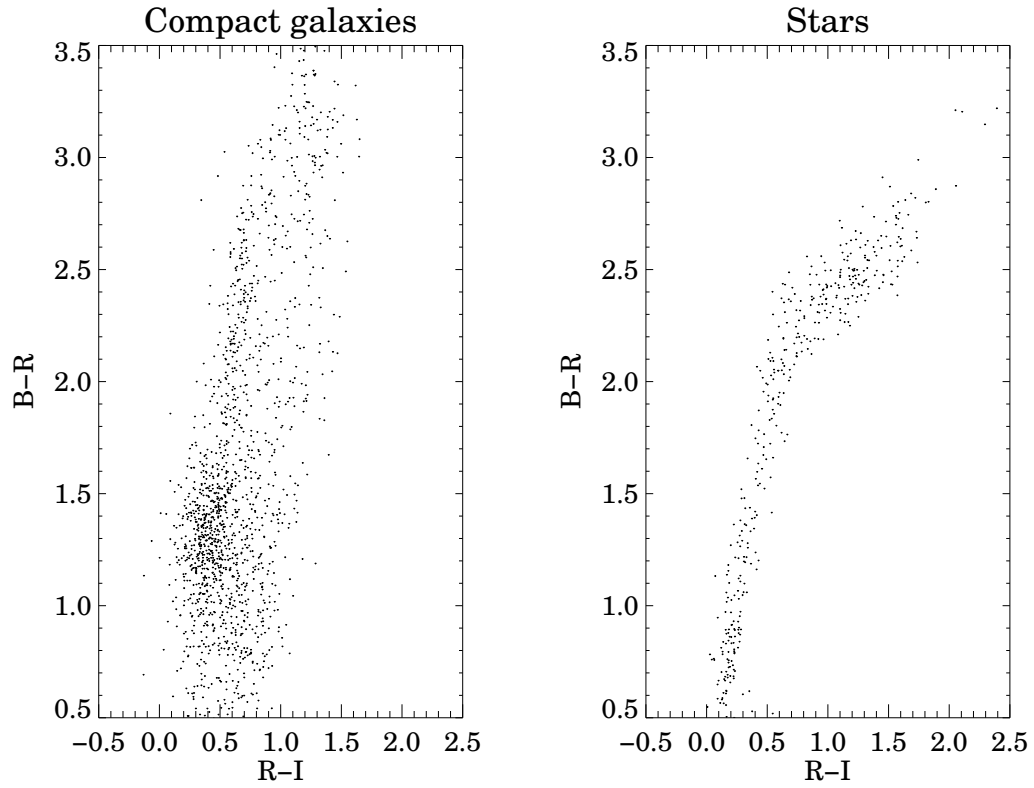


FIG. 3.— Color-color distribution for compact galaxies and stars in one pointing; these distributions are used to define the probability that a given object is a galaxy.

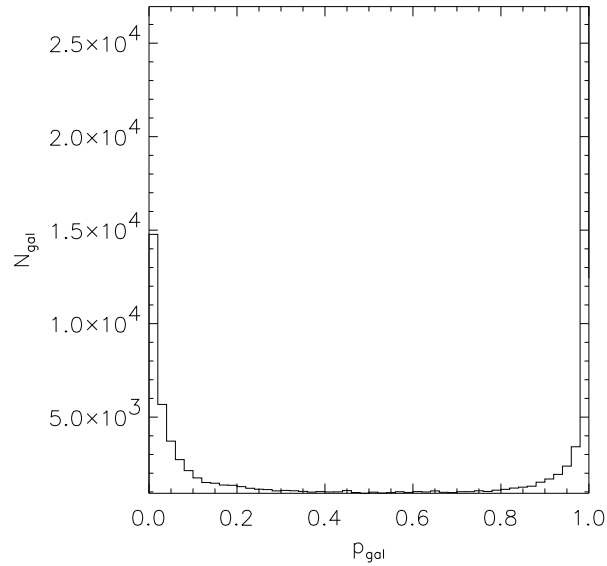


FIG. 4.— Probability distribution that a compact object is a galaxy for data in all pointings. The distribution is quite bi-modal; most compact objects are clearly classified as stars or galaxies.



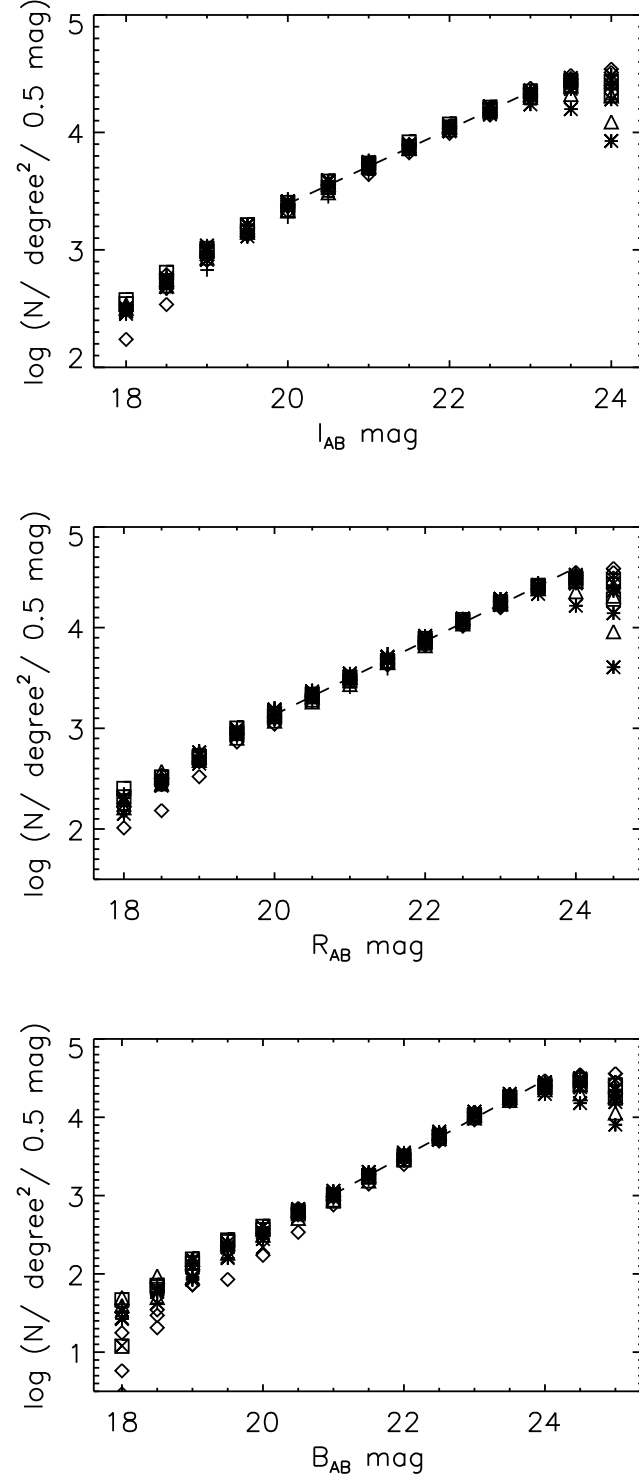


FIG. 5.— Galaxy counts for  $B_{AB}$ ,  $R_{AB}$ , and  $I_{AB}$  bands. The dotted lines are linear fits discussed in the text (see Section 4).

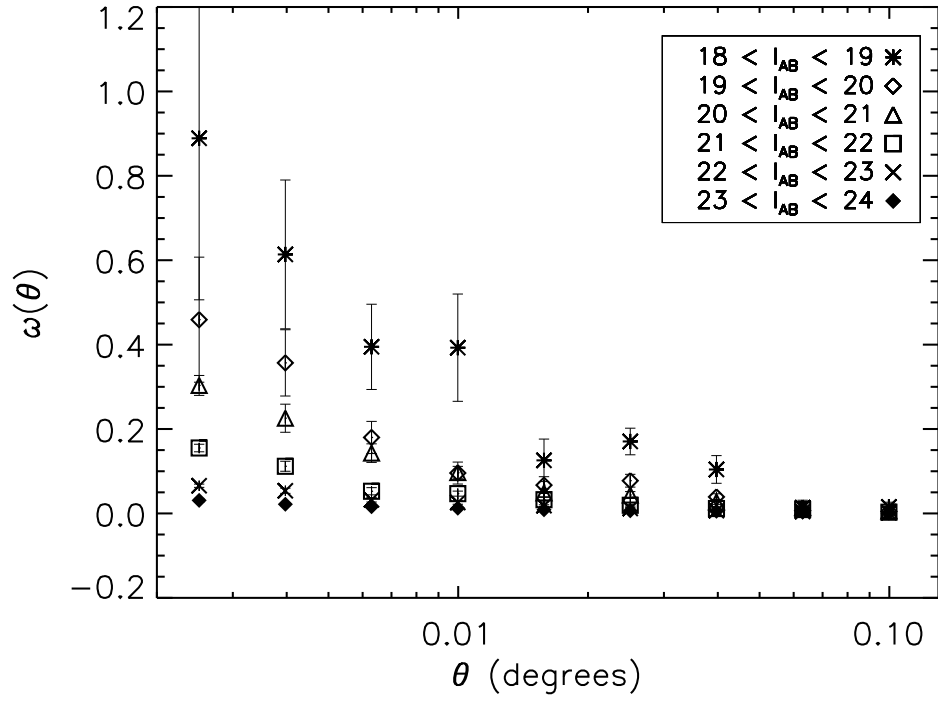


FIG. 6.— The angular correlation function,  $\omega(\theta)$ , measured for independent  $I_{AB}$  magnitude bins, shown on scales  $\sim 7'' - 6'$ .

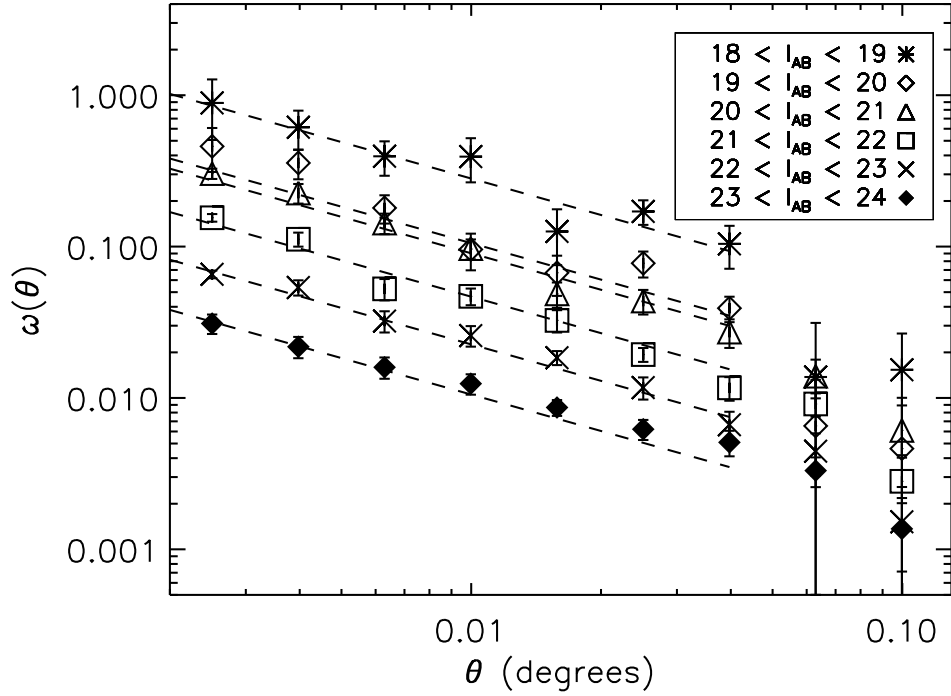


FIG. 7.— The angular correlation function,  $\omega(\theta)$ , plotted on a log scale for different  $I_{AB}$  magnitude ranges. Power law fits for  $\omega(\theta) = A_w \theta^\delta$  on scales  $\sim 7'' - 2'$  are shown as dashed lines, assuming a constant slope of  $\delta = -0.8$ .

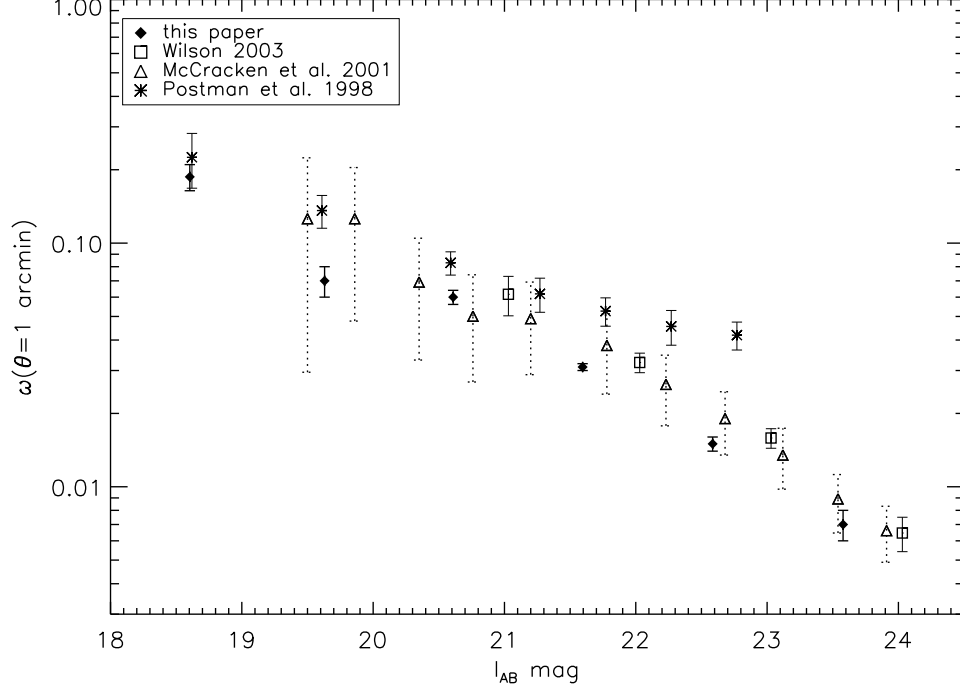


FIG. 8.— The amplitude of  $\omega(\theta)$  measured at  $1'$  shown as a function of the median  $I_{AB}$  magnitude, assuming a slope of  $\delta = -0.8$ . Results from McCracken et al. (2001) and Wilson (2003) are plotted as well, with dotted error bars for clarity.

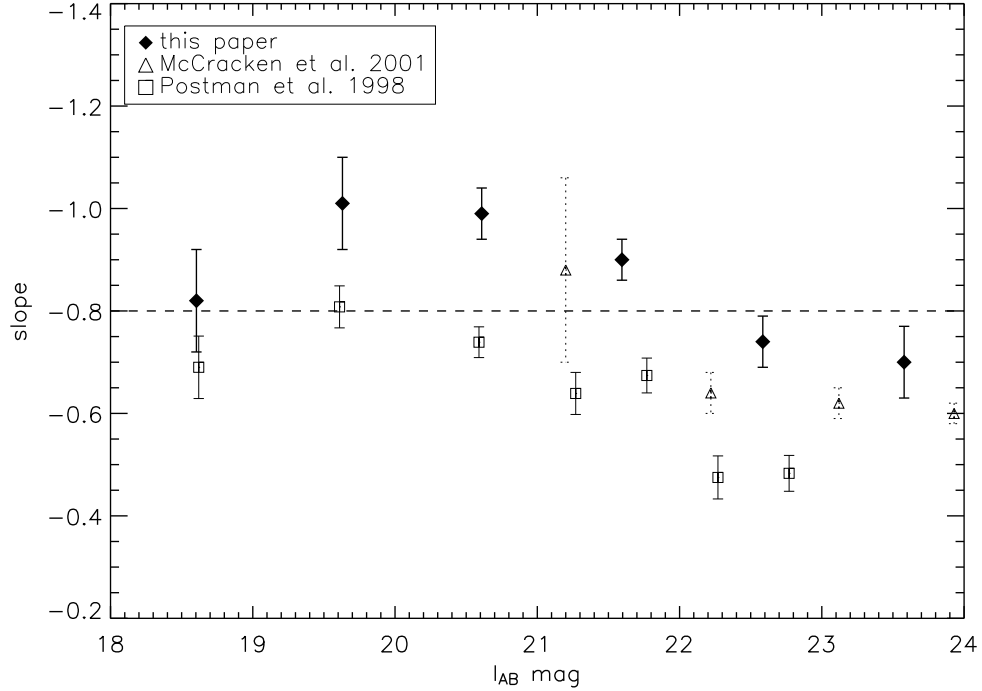


FIG. 9.— The best-fit slope,  $\delta$ , of  $\omega(\theta)$  as a function of median  $I_{AB}$  magnitude. The slopes are fit on scales of  $\sim 7'' - 3'$ . Results from McCracken et al. (2001) and Postman et al. (1998) are shown for comparison.

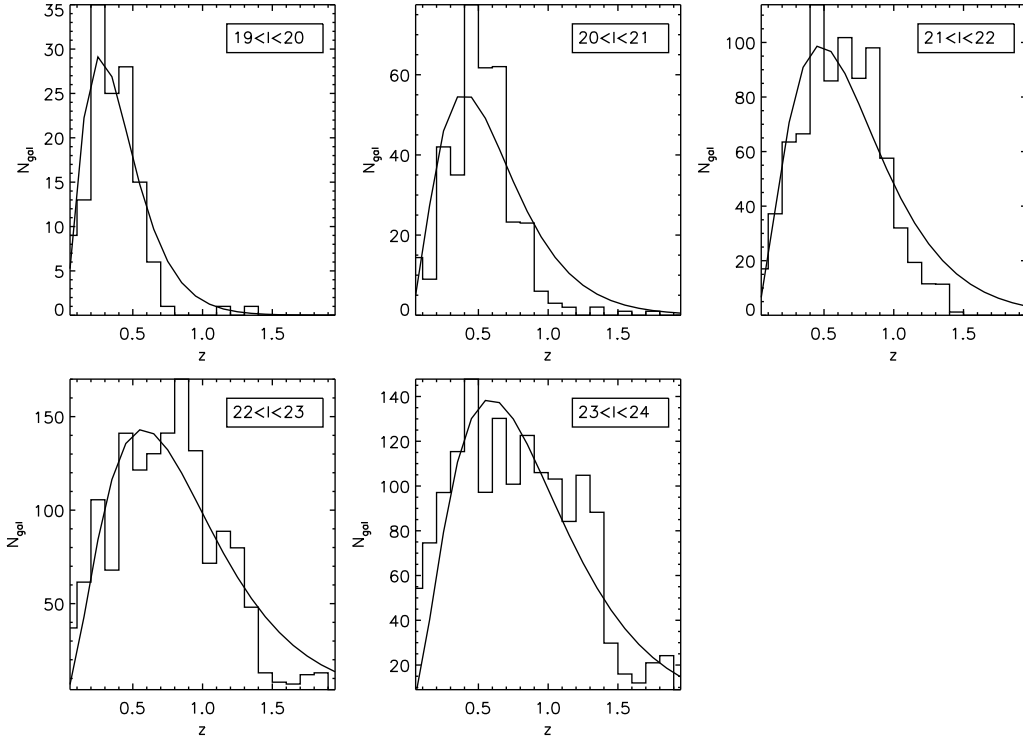


FIG. 10.— Redshift histograms of galaxies in the early DEEP2 Redshift Survey data for independent  $I_{AB}$  magnitude ranges. Fits for  $dN/dz \propto z^2 \exp(-z/z_0)$  are plotted as solid curves, and values for  $z_0$  are listed in Table 3. The mean redshift in each magnitude range is  $3z_0$  and the median redshift is  $2.67z_0$ .

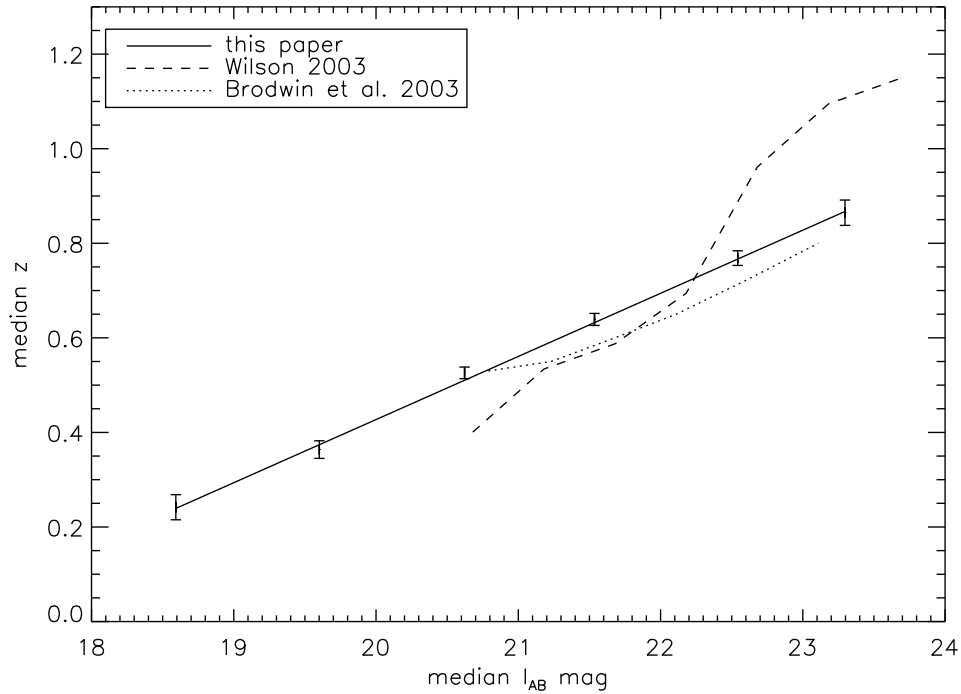


FIG. 11.— Median redshift as a function of  $I_{AB}$  magnitude for data from the DEEP2 Redshift Survey, using the fits shown in Figure 10, where the median redshift is  $2.67z_0$ . The solid line is a linear fit to the data:  $z_0 = -0.84 + 0.050 \text{ median } I_{AB}$ . Results from two recent surveys are also shown.

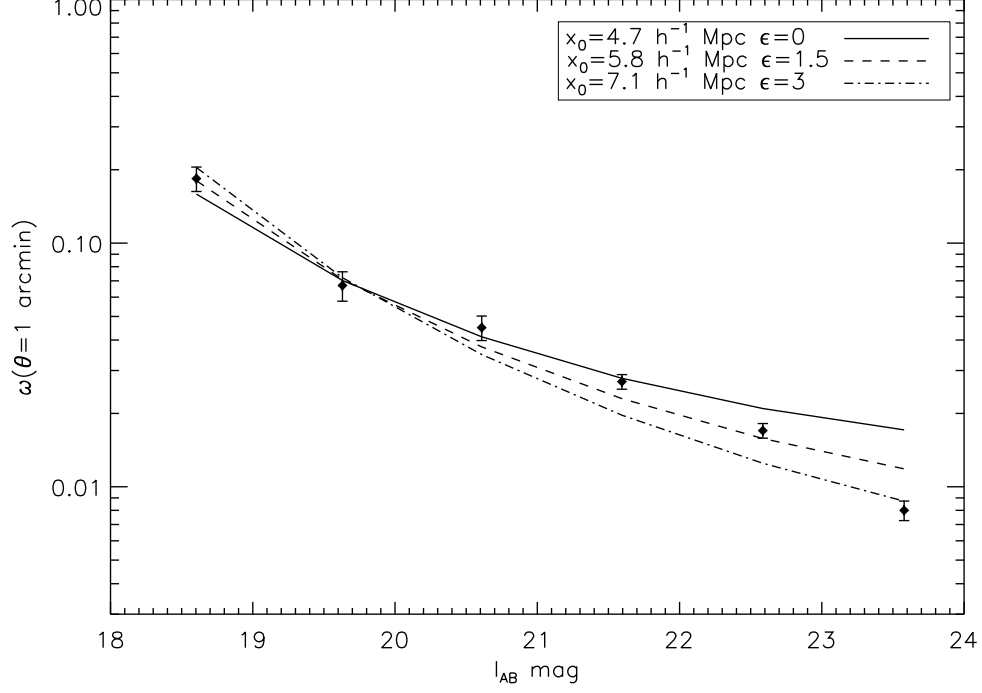


FIG. 12.— The amplitude of  $\omega(\theta)$  at  $1'$  as a function of the median  $I_{AB}$  magnitude compared with predictions for different values of the local clustering scale-length,  $x_0(0)$ , and an evolutionary parameter,  $\epsilon$ , such that  $x_0(z) = x_0(0)(1+z)^{-(3+\epsilon-\gamma)/\gamma}$ .

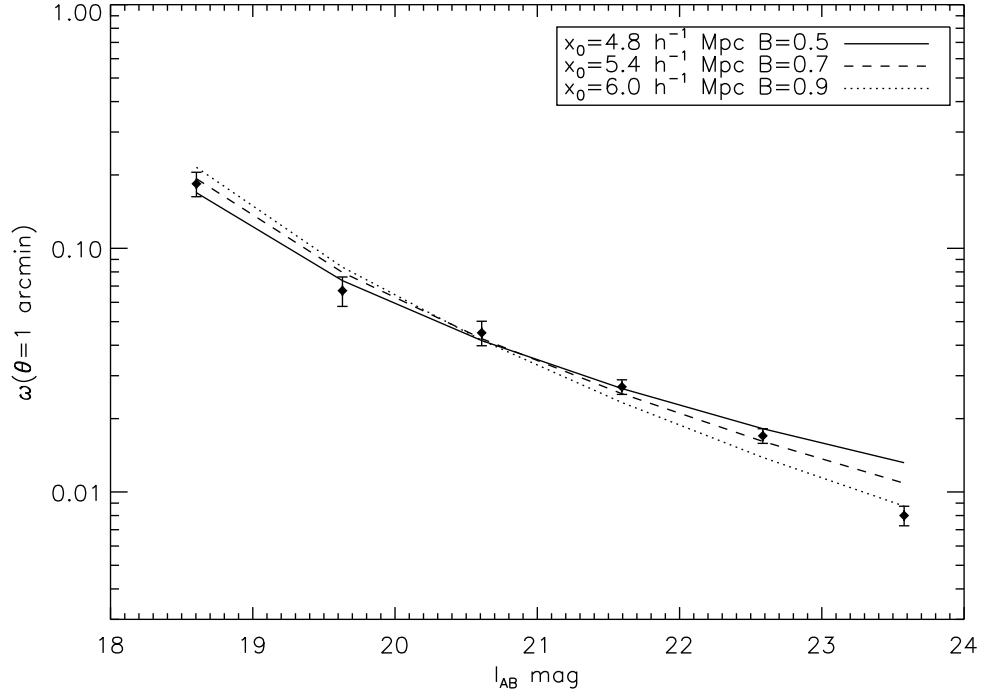


FIG. 13.— Same as Figure 12, for a model in which  $x_0(z)$  evolves linearly with redshift:  $x_0(z) = x_0(0)(1 - Bz)$ , for  $z \sim 0 - 1.5$ .

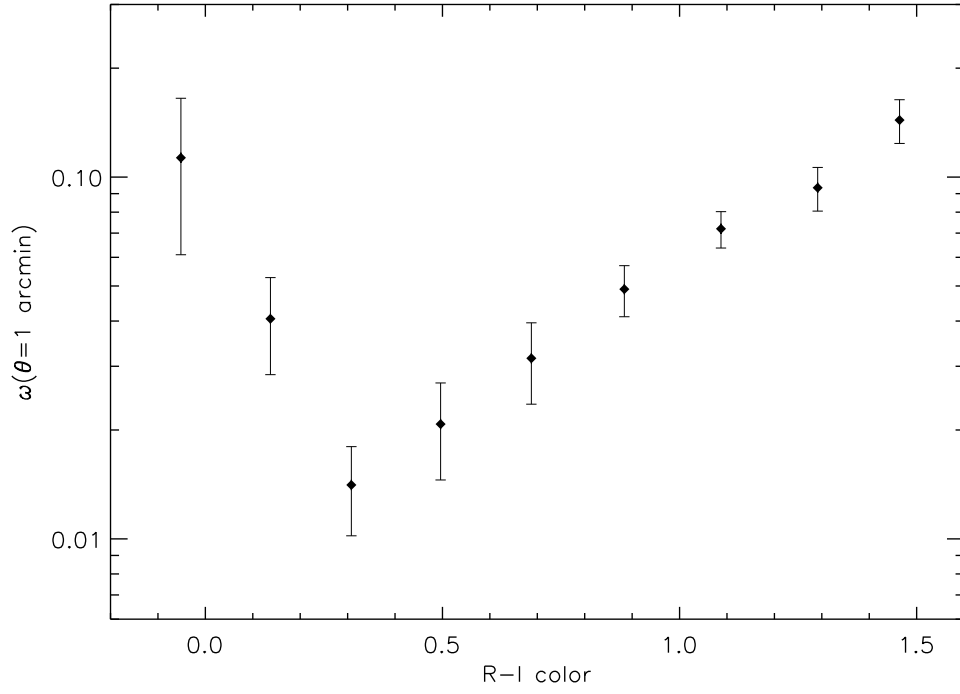


FIG. 14.— The amplitude of  $\omega(\theta)$  measured at  $1'$  shown as a function of  $(R-I)$  color, where the slope has been measured simultaneously (see Figure 15).

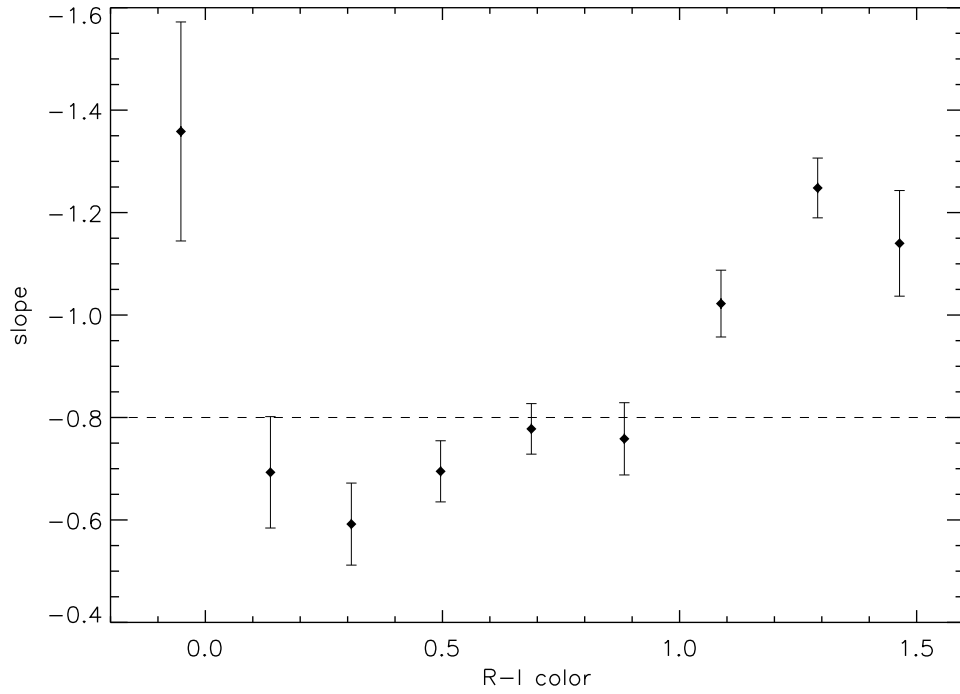


FIG. 15.— The best-fit slope,  $\delta$ , of  $\omega(\theta)$  as a function of  $(R-I)$  color.

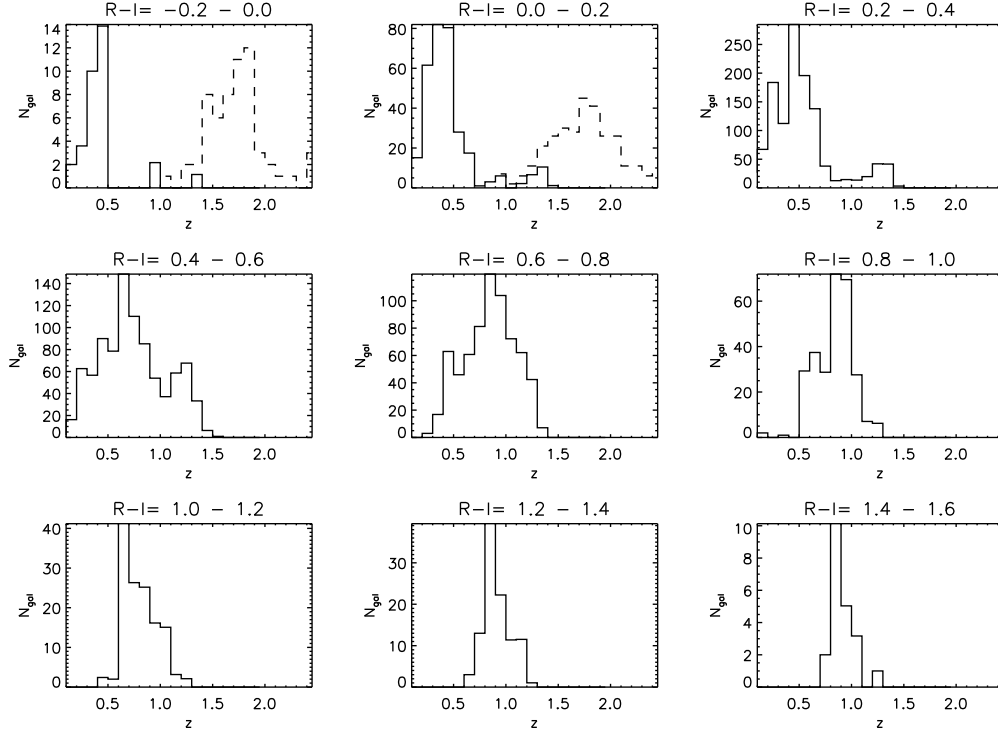


FIG. 16.— Redshift distribution of DEEP2 EGS sources as a function of  $(R-I)$  color. The dashed lines for the two upper left plots show the assumed redshift distribution for galaxies at  $z > 1.45$  (see text for details).

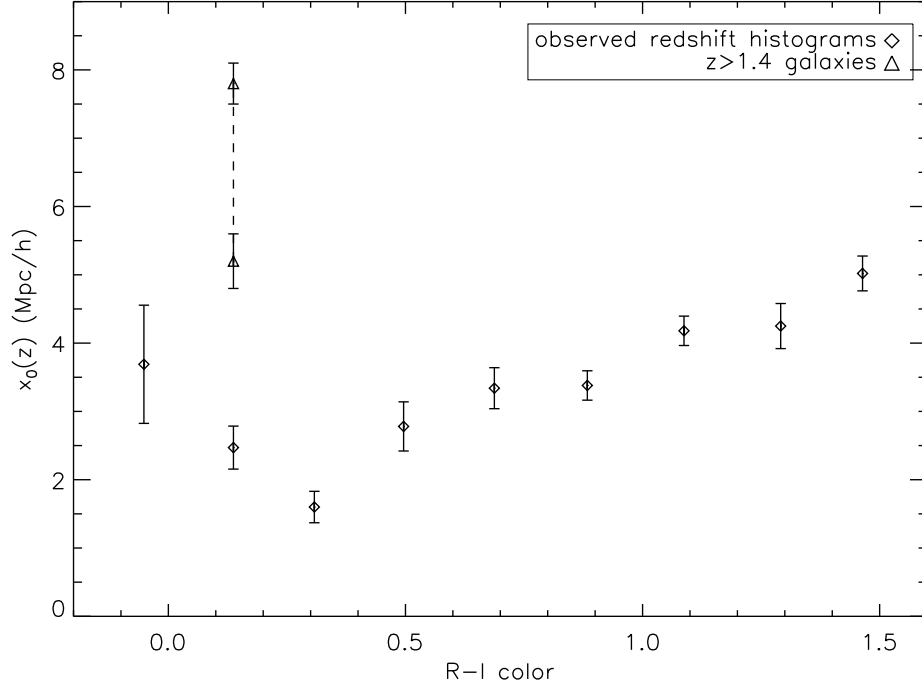


FIG. 17.— The comoving scale-length  $x_0(z)$  as a function of observed  $(R-I)$  color. In addition to the scale-length derived using the observed redshift distributions shown in Figure 16, we also plot values of the scale-length derived for  $z \sim 1.7$  galaxies (see text for details).